Electron Dosimetry in Heterogeneous Media

by

Kenneth R. Hogstrom, Ph.D.
Department of Radiation Physics
The University of Texas M. D. Anderson Cancer Center

I. INTRODUCTION

Electron beam dose distributions are clinically useful because of the relatively uniform dose between the surface and the therapeutic depth (R_{80} to R_{90}), which can be controlled by varying the beam energy. The sharp falloff of dose with depth beyond the 80% isodose surface permits sparing of critical structures distal to the target volume. Such a dose distribution results from normal incidence on water (c.f. Figure 1) and presents an opportunity for treating a superficial target volume with an appositional radiation field. However, the presence of tissue heterogeneities can modify such a dose distribution so that it is not as clinically desirable. A tissue heterogeneity in the present context is defined as either a surface irregularity or any volume within the patient that contains tissue with a composition or density different from that of muscle. To properly plan electron treatment, it is necessary to understand the types and magnitudes of dose perturbations due to tissue heterogeneities. The purpose of the present paper, an update of a previous review by Hogstrom (1983), is to categorize and review the effect of common tissue heterogeneities.

It is desirable to have a treatment planning computer capable of accurately computing dose in the presence of tissue heterogeneities. This is not always the case; therefore, one must know how to interpret the accuracy of one's planning system's dose algorithm. Accuracy of the Hogstrom pencil beam algorithm has been discussed in some detail (Hogstrom et al., 1993; Hogstrom and Steadham, 1996). Also, the art of treatment planning allows the effects of tissue heterogeneity to be reduced and in some cases eliminated. Both of these topics are discussed in subsequent papers.

II. EFFECT OF HETEROGENEITIES ON TREATMENT AIMS

The effect of heterogeneities on electron beam dosimetry is somewhat different than that on photon beam dosimetry. In photon beam dosimetry the most significant influence of tissue heterogeneities is to change the attenuation of the primary beam, resulting in a decrease or increase of the dose at depth. The resulting dose distributions may not change significantly in shape, but isodose values may change by several percent. Therefore, if one is going to start prescribing doses based on dose distributions that have been corrected for heterogeneities, whereas previous dose prescriptions have been based on noncorrected dose distributions, then it becomes necessary to know the mean difference between the doses calculated by the two methods. A different dose prescription will be necessary in order that patients would on the average, receive the

same dose that previous patients, whose dose was calculated assuming patient homogeneity, had received. An appreciation of this concept is required by both the physicist and radiation oncologist if CT-corrected dose distributions are to be use for photon beam treatment planning.

Contrastingly, electron beams are characterized by a sharp fall-off in dose distal to the depth of R_{80} (depth of the 80% dose) and by a relatively uniform dose distribution between the surface and the therapeutic depth (R_{80} to R_{90}). Therefore, dose is normally prescribed to the dose maximum (100%) or an isodose contour in the range from 80%-90%. The radiation oncologist is then interested in the geometric coverage of the 80%-90% isodose contour and the uniformity of dose within the treatment volume defined by that contour. Heterogeneities within the treatment volume can potentially lead to the following clinical problems:

1. Geographic miss – heterogeneities denser than muscle, such as bone, can shift the 80%-90% isodose lines toward the surface, possibly resulting in a geographical miss along part of the distal region of the target volume.

2. Overdose to distal critical structures – structures distal to air or lung may be receiving more dose than expected due to the greater depth of penetration of electrons passing through tissue of less than unit density, such as air or lung.

3. Nonuniform dose – dose within the treatment volume may have hot or cold spots (volumes of increased or decreased dose) due to sidescatter nonequilibrium. Such dose nonuniformity could result in normal tissue complications or tumor regrowth, respectively. One should be aware that for every hot spot there exists a cold spot, and vice versa.

III. TYPICAL HETEROGENEITY EFFECTS IN ELECTRON TREATED PATIENTS

A. Skin Surface Irregularities

Skin surface irregularities can be classified into oblique surfaces and irregularly shaped surfaces.

1. Sloped Surfaces

If the skin is sloped so that the electron beam is obliquely incident, then three effects are observed – (1) a change in depth dose, (2) a change in dose homogeneity within the treatment volume (80-90% isodose contour) due to the effect of inverse square and patient scatter, and (3) a change in penumbra width due to increased (or decreased) distance between the surface and the beam defining collimator.

The change in depth dose that results from oblique incidence of a broad electron beam has been explained by Ekstrand and Dixon (1982). Figure 2 compares central-axis depth dose for a 9-MeV electron beam for angles of 0°, 30°, 45°, and 60° from normal incidence. Comparison of depth-dose properties for non-normal incidence relative to those for normal incidence show (1) increased surface dose (D_s), (2) decreased depth of maximum dose (R_{100}), (3) increased maximum dose (D_{100}), (4) decreased therapeutic depth (R_{90}), and (5) increased depth of maximum penetration (R_{max}). The magnitude of these changes increases with increased angle from normal incidence. For example, at 45° incidence, R_{100} decreases from 1.8 cm to 0.5 cm, D_{100} increases from 100% to 109%, R_{90} decreases from 2.8 cm to 1.8 cm, and R_{max} increases from approximately 4.7 cm to 6.5 cm. D_s should increase from approximately 90% to 100%, similar to changes at depth = 1 cm. The fact that the data does not show this likely illustrates an error in the 45° surface data.

The decrease in R_{90} is likely to be the most significant clinically. R_{90} is reported along central axis of the beam; however, the distance of the 90% isodose contour from the surface is actually less, given by $R_{90} \bullet \cos \theta$. For example at 45°, R_{90} decreased from 2.8 cm to 1.8 cm, whereas the distance between the surface and the 90% isodose contour decreased from 2.8 cm to 1.3 cm.

As the electron beam is a diverging beam, the dose also decreases as distance from the source increases. This is clearly observed in Figure 4, which plots the isodose contour for a 13-MeV electron beam incident 45° from normal. Note that on central axis that R_{100} increases from 100% to 110%. However, the dose under the surface closer to the source increases to approximately 120% as a result of inverse square, and the dose under the surface farther from the source decreases to approximately 100%. Measured data has been reported for angled incidence by Hogstrom et al. (1983) and Shiu et al. (1992) and for circular anatomy by McKenzie (1979) and Wooden et al. (1996).

All of these effects are illustrated in Figure 3, which shows the dose resulting from a broad 9-MeV beam irradiating a calf phantom (Wooden et al., 1996). Note that the depth of 90% isodose contour decreases from approximately 1.5 cm on central axis where there is normal incidence, to 0 cm laterally, where the angle of incidence is approximately 90° (tangent to the surface). Also, note that there is a small region of dose that exceeds 100% even though the overlying surface is at an extended SSD. The decrease due to inverse square is offset by the increase in dose due to non-normal incidence.

Also illustrated in Figure 4 is the penumbra width increasing proportionally with distance from the beam defining collimator. In this example, the collimator is located 10 cm above the 100-cm SSD, i.e. a 90-cm source-to-collimator (SCD) distance. Hence the penumbra on the left is 15-cm from the collimator, three times the distance than the 5-cm distance on the right, resulting in a penumbra width approximately three times greater.

It is clear from these data that normal incidence to the patient surface is best. Angles of incidence greater than 30° begin producing clinically undesirable depth-dose and penumbra effects.

2. Surface Protrusions

Irregularly shaped surfaces, classified into protrusions and depressions, can have significant impact on the lack of homogeneity of dose. Illustrated in Figure 5, the dose beneath a 2-cm wide by 2-cm high protrusion is calculated for a 13-MeV beam. Beneath and lateral to the protrusion is a volume of increased dose, showing dose values in excess of 110%. This is caused by electrons that are scattered away from central axis by the protrusion not being replaced by electrons scattering back towards central axis by the air lateral to the protrusion. Rather those electrons passing through air continue traveling in the forward direction, adding to the scattered electrons and resulting in a volume of increased dose (hot spot). Correspondingly, there is a volume of decreased dose (cold spot) beneath the lateral protrusion and just inside its edge. To conserve energy (and likewise integral dose), there is always a volume of decreased dose (cold spot) to correspond to a volume of increased dose (hot spot) and vice versa. For a protrusion, the region of increased dose is in the volume below and outside its periphery, and the region of decreased dose is in the volume below and inside the periphery. Clinical examples of a protrusion are the nose and the external ear. Figure 6 illustrates this effect for the nose by comparing the dose distribution calculated considering multiple Coulomb scattering (MCS) with that calculated not including MCS. This clinical case will be discussed in greater detail later when internal air cavities are discussed.

3. Surface Depressions

Illustrated in Figure 7, the dose beneath a 2-cm wide by 2-cm deep depression is calculated for a 13-MeV electron beam. Beneath and lateral to the depression is a volume of decreased dose, showing dose contours as low as 80%. This is caused by electrons being scattered by the water between 0 and 2 cm depth towards central axis not being replaced by electrons scattering away from central axis due to air in the depression. Rather electrons continue traveling in the forward direction and add to the scattered electrons, resulting in a volume of increased dose. Correspondingly, there is a volume of decreased dose beneath the lateral depression and just outside its edge. For a depression, the region of increased dose is in the volume below and inside its periphery, and the region of decreased dose is in the volume below and outside the periphery. The distribution of the dose nonuniformity is highly dependent on the beam energy and geometry of the depression. As measured by Perry and Holt (1980), and illustrated in Figure 8, beam profiles beneath a depression 1×1 cm^2 cross-section and 2-cm deep for an 11-MeV beam show dose increases in doses as great as 130%. For smaller depression such as the ear canal, calculations show dose deep to the ear canal being as great as 160% as opposed to 125% when the canal is filled with water

(Morrison et al. 1995). Note that the 125% is due to the surface protrusion of the anti helix, concha, and tragus of the external ear.

B. Internal Tissue Heterogeneities

1. Air Cavities

Air cavities within the patient have similar effects on the dose distributions as do surface depressions. In Figure 9, calculated isodose curves for a 17-MeV electron beam in water are compared with those with a 2×2 cm^2 cross-sectional air cavity 2 cm below the surface. This illustrates how the dose distribution in the shadow of the air cavity (1) penetrates deeper as a result of electrons losing essentially no energy in traversing the air and (2) has a volume of increased dose due to the lateral scattering. Just outside the shadow of the air cavity is the corresponding volume of decreased dose. Now how the volume affected by the air cavity flares with depth as a result of multiple Coulomb scatter. Dose distributions calculated by conventional pencil-beam algorithms, e.g., Figure 9, underestimate the scattering effect of the air cavity. This is illustrated in Figure 10, which compares calculated with measured dose distributions from a 20-MeV electron beam for a 1×3 cm^2 air cavity located 1-cm below the surface. Air cavities encountered in clinical situations are typically in the head and neck, e.g. maxillary sinuses and nasal cavities. The nasal cavities are characterized by being long and narrow with respect to the direction of the incident beam. This case is illustrated in Figure 11, which shows the dose distribution resulting from irradiation of a 2D-nose phantom using a 13-MeV electron beam. Of particular clinical significance is the low dose to the septum, which in the patient after which the phantom was modeled, contained tumor. In such cases, electrons are continually removed from the septum with depth as there is no tissue in the nasal passageway to scatter electrons back into the septum. This results in measured dose to the septum of 86% and 73% at a depth beneath the nose of 3.3 cm and 4.2 cm respectively, which correspond to a depth dose in water of 99% and 84% respectively. As seen by calculated dose in Figure 11, the pencil-beam calculated overestimated the decreased dose predicting 94% and 86% respectively.

Air cavities are often quite complex, particularly in the head in the presence of multiple sinuses. The impact on the dose distribution depends on beam energy and on the location and geometry of the air cavities. This complexity makes us depend on dose calculation for purposes of treatment planning in such cases.

2. Lung

Electrons are not typically used to treat tumors in the lung, but are frequently used to treat the chest wall or internal mammary chain overlying lung. Typical tumor doses are 50-60 Gy and doses of 30 cGy have a 5% probability of causing acute and chronic pneumonitis in lung within 5 years after treatment. Therefore, the primary concern of lung is its impact on the depth falloff portion of the electron dose distribution in lung.

The influence on lung has been studied by a number of investigators as they parameterized the dependence of AET and CET on energy, depth, and field size (ref). Figure 12 illustrates the depth dose for a 9-MeV electron beam with lung equivalent material downstream of a 3-cm thick chest wall. Note that in water that R_p of a 9-MeV beam is approximately 4.5 cm, 1.5 cm distal to the 3 cm depth. However, with the lung-equivalent material, the practical range is approximately 7.5 cm, 4.5 cm distal to the 3 cm depth. This is consistent with the 0.33 density of the lung equivalent material.

To see the clinical implication, Figure 13 compares the dose distribution without lung correction to that with lung correction for a patient receiving chest wall irradiation. In this case, the beam energy is optimal, i.e. the 90% isodose contour closely tracks the chest-wall-lung interface. Still, considerable lung is irradiated by the 40% isodose contour, which corresponds to 20 Gy. Note how neglecting the density of lung grossly underestimates the volume of lung irradiated to the critical 20 Gy dose. This effect can be more significant if the thickness of lung is highly variable and the energy is selected such that R_{90} exceeds the maximum depth of the target volume. Also, the finite steps in accelerator energy can result in the 90% isodose contour lying well inside the lung. For example, it is possible for there to be as much as a 3-MeV excess in energy (typical energy increment between successive electron energies on some machines). This corresponds to 1.5 cm extra penetration in unit density tissue, but 4.5–6.0 cm increased penetration in lung.

3. Bone

Bone is one of the more frequently encountered inhomogeneities encountered when treating with electrons. There are three regions which are influenced by bone – the adjacent upstream tissue, the dose in bone, and the dose in tissues distal to bone.

a. Backscatter from Bone – Whenever electrons encounter an inhomogeneity with a higher atomic number, there is an increase in dose to muscle due to backscattered electrons. This dependence is usually characterized by the electron backscatter factor, EBF, which is defined as the ratio of dose with the bone to dose at the same point with the bone replaced by unit density, water or muscle. It is well known that the EBF for lead can be as great as 1.6 at 5 MeV and its use for internal collimation without protection can cause significant clinical problems (Klevenhagen et al., 1982; Lambert and Klevenhagen, 1982). The backscattered dose (EBF-1.00) decreases approximately exponentially with distance upstream of the tissue-lead interface, with a HVL ranging from 2.3 to 4.6 mm for mean electron energies of 3 MeV to 10 MeV incident on the interface. Backscattered electrons from bone should be less than backscatter from calcium (Z=20) for which the EBF is approximately 1.18 at 5 MeV. At the M. D. Anderson Cancer Center, no adverse clinical reactions have been observed as result of backscatter from bone or teeth. This is a result of the EBF being 1.05 or less according to the study of Shiu and Hogstrom (1991). As seen in Figure 14, the EBF reaches a maximum with as little as 4 mm of hard bone. For energies ranging from 2 MeV to 13 MeV, the EBF varied from approximately 1.05 to 1.02. This encompasses the

energy range to which bone in the target volume might receive full dose. From these results, it can be concluded that the maximum increase in dose due to backscatter is 5%, hence explaining why no adverse clinical reactions are observed.

b. Dose in Bone – Early experiences with orthovoltage x-rays in which there is a clinically significant increase in dose to bone due to the kerma effect (John and Cunningham, 1983) has made radiation oncologists alert to the potential for new types of radiation to produce increased dose in bone. In the case of electrons, increased dose to marrow in bone has been shown to be 7% or less by Shiu and Hogstrom. This is seen in Figure 15, which shows the measured depth-dose distribution passing through a 1.3-cm thick slab of hard bone. In such cases, the increase in dose is due to the increased scatter in bone relative to muscle. Increased scatter results in an increased fluence of electrons, the same phenomenon that produces the slow buildup in electron depth dose in water (Hogstrom, 1991). Because bones encountered by electron beams usually have a softer center (marrow), it is felt that dose in most bones will be less than that measured in 1.3-cm thick bone material as was used by Shiu and Hogstrom. These data are consistent with experiences at the M. D. Anderson Cancer Center. Treatment with electrons for numerous sites and dating back to the 1970's under the late Dr. Norah duV Tapley (Tapley, 1976) have resulted in no reported bone necrosis. Note that the data of Shiu and Hogstrom refuted measurements by Prasad et al. (1984), which they concluded were made incorrectly resulting in erroneous reports of increases in bone dose as great as 17%.

c. Dose in Shadow of Bone – As electrons penetrate bone, they lose energy at a more rapid rate per centimeter as a result of increased density and they experience greater MCS as a result of a higher atomic number. This results in isodose surfaces being shifted towards the bone and in hot/cold spots under the lateral boundaries respectively.

From a clinical perspective, the shifting of the 90% isodose surface, illustrated in Figure 16, can be significant. This is illustrated clinically in Figure 17 where the mandible causes a shift towards it of approximately 8 mm of the 90% isodose line of an 18-MeV electron beam used to treat carcinoma of the buccal mucosa and retromolar trigone. Also illustrated in Figure 16 is a hot spot ($\approx$ 104%) lateral to the bone-water interface and a corresponding cold spot ($\approx$ 96%) under the bone. Measured phantom data at 17 MeV and 20 MeV in Figures 18 and 19 respectively show the hot/cold spots to be approximately $\pm$ 15% and $\pm$ 5% and for pencil-beam calculated dose to slightly underestimate measured values. Because bones are neither solid nor are their edges as sharp, hot/cold spots in patients are usually of less magnitude and of little clinical concern.

Erroneous data in the literature has often implied larger hot/cold spots when measurements were made using aluminum, which is a poor substitute for bone, being too dense and having too great of an atomic number. Another misconception in the literature is that ribs have significant effect on the dose distribution. Ribs consist of a very thin bony wall, which has an almost undetectable effect on the dose distribution.

Another patient site where the influence of bone can be very significant is the treatment of the spinal axis with electrons, a technique referred to as craniospinal irradiation. Maor et al. (1985) reported that R_{90} is shortened approximately 4 mm by the spine and must be considered in planning the treatment energy. Also, the protrusion of the spinous processes creates hot/cold sports. This is illustrated in Figure 20, which shows the dose under T11-L4 to vary between 95% and 107%. Dose to the spinal theca is usually prescribed to the 90% isodose contour, so that the hot spots can be as great as 118 % of the prescribed dose.

V. METHODS FOR SUPPRESSING THE EFFECT OF TISSUE HETEROGENEITIES ON THE ELECTRON DOSE DISTRIBUTION

The effect of tissue heterogeneities on the electron dose distribution can hinder the achievement of treatment objectives. Therefore, as part of the treatment planning process, methods must be applied which can reduce their effect allowing treatment objectives. Three methods often employed are (1) change in beam direction, (2) mixing with photon beams, and (3) using electron bolus.

It is clear that normal incidence can reduce the effects due to a sloping surface. If abutting beams are involved, the tradeoff may be that changing the angulation of one beam may increase problems with abutment dosimetry, as is the case for chest wall treatment. Dose distributions of photon beams are less influenced by the heterogeneity. However, they deliver less entrance dose and additional exit dose, and these efects must be weighed. (Fields and Hogstrom, 1981) Probably the most useful technique for removing effects of tissue heterogeneities is the use of electron bolus (Hogstrom, 1991; Low et al., 1992), which can remove surface irregularities, increase surface dose, and control penetration of the 90% isodose surface. The use of these techniques will be discussed further in the section on treatment planning.

VI. SUMMARY AND RECOMMENDATIONS

Tissue heterogeneities clearly impact the electron dose distributions. Irregular patient surface can create significant dose heterogeneity in the target volume. Air cavities result in deeper penetration of the isodose surfaces in its shadow and hot/cold spots inside/outside its shadow. Dose penetrates 3-4 times deeper in lung so that energy selection is significant in chest wall irradiation. Backscatter dose from bone, and increased dose in bone are of no consequence. The geometric coverage of the distal 90% isodose surface as it is shifted toward the bone can be important in energy selection. In craniospinal irradiation the spinous processes create hot/cold spots if ± 10% and greater.

The impact of tissue heterogeneities on the dose distribution is clearly significant. Because of the varying and complex shape of these heterogeneities, the resulting dose distribution can be appreciated only by having access to a treatment planning system with a pencil-beam or other equally accurate dose algorithms.

Therefore, it is recommended that electron beam treatment planning account for patient heterogeneity by (1) obtaining a CT scan of the patient, (2) calculating dose using a pencil-beam or more accurate algorithms, and (3) calculating dose in three-dimensional space or at the least from multiple transverse planes.

Only with this process can the radiation oncologist be assured of avoiding geographical miss, overdose to underlying critical structures, or unacceptable dose homogeneity (hot/cold spots). Of course the use of bolus, change in beam direction, and or photon beam mixing may also be required to achieve the desired dose distribution.

Appendix A
Physical Processes In Which Tissue Heterogeneity Impacts Dose Distribution

There are three dominant physical processes through which the dose distribution is altered in patients irradiated by electron beams: range modification, sidescatter, and backscatter. The three effects normally influence the dose at a point simultaneously so that it is difficult to isolate one process and make a dose calculation considering only that process. However, for the sake of discussion, let us consider each process individually in some idealized cases.

1. Range Modification

The most significant of these processes is range modification. As electrons pass through matter, they lose energy by undergoing Coulomb scattering with other atomic electrons. For electrons at therapeutic energies and in tissue, the energy loss is primarily due to nonradiative processes, and the collisional energy loss per unit path length as given by ICRU 35 (1984) is

$$S_{coll} = n_e \frac{2\pi r_e^2 m_e c^2}{\beta^2}\left\{\log\left[\frac{\tau^2(\tau+2)}{2(I/m_e c^2)^2}\right] + F(\tau) - \delta\right\} MeV \bullet cm^{-1}, \qquad (1)$$

where:

n_e = electron density = $N_A \left(\frac{Z}{A}\right)\rho$

ρ = physical density
N_A = Avogadro's number
Z = atomic number
A = atomic weight

and the remaining quantities are given in ICRU 35. The point of interest is that the primary influence of the medium upon the stopping power is the electron density. For the moment assume that electrons travel in a straight line. Then the range of the electrons of initial kinetic energy E is given by

$$R = \int_{E_o}^{0} \frac{dE}{S_{coll}}, \qquad (2)$$

so that the range in a particular tissue-like material relative to that in our reference material (usually water) is given by

$$R = \left(\frac{R}{R_{H_2O}} \right) R_{H_2O} \approx \left\{ \frac{n_e^{H_2O}}{n_e} \right\} R_{H_2O}. \tag{3}$$

More specifically, if we define the water equivalent depth in two media as that depth where the average energy of the electron beam is identical, then it can be shown

$$d_{eff} = d_{H_2O} = \left(\frac{n_e}{n_e^{H_2O}} \right) d = \rho_e \, d \tag{4}$$

where ρ_e is defined as the electron density relative to that of water. The effective depth of a mixture of tissue is given by

$$d_{eff} = \sum_{i=1}^{N} \rho_e^i . \Delta_i , \tag{5}$$

where Δ_i is the thickness of each medium. If the physics of the situation were this simple, then we might expect that the dose distribution in heterogeneous tissue could be calculated from the dose distribution measured in water by simply correcting the dose at the equivalent depth in water for inverse square and any geometric dependence of the penumbra, namely

$$D(X,Y,d) = D^{H_2O}(X',Y',d_{eff}) \left(\frac{SSD + d_{eff}}{SSD + d} \right)^2 . \tag{6}$$

The range of electrons is considerably modified by straggling. There are two types of straggling: path length straggling and energy straggling. Energy straggling refers to the statistical nature of energy loss resulting in a distribution of the range due to the average energy loss along the particle tracks being different. Path length straggling considers the fact that electrons do not travel in straight lines, but are deflected constantly by multiple Coulomb scattering with the nucleus. This effect results in the range having some distribution whose shape depends upon the material and the energy of the electron. The physical laws of these processes is beyond the scope of this work; however, this results in the water equivalent depth of a medium becoming a more ambiguous quantity, since the energy distributions of the two media at depths corresponding to the same average energy will no longer be identical. This is manifested in the dosimetry of central-axis depth dose by neither the ranges nor the

shapes of the dose falloff on the distal edge of two beams scaling according to their relative electron densities (i.e., eqn. 6). Consequently, it may be more preferable to define the effective depth in terms of a relative range, combining equations (3) and (4),

$$d_{eff}^{H_2O} = \left(\frac{R}{R_{H_2O}} \right) d \quad . \tag{7}$$

Measurements of depth-doses in bone and lung tissue substitutes have been made by Laughlin et al. (1965) Their data show a depth dependence of the constant of proportionality that relates effective depth to physical depth; however, a single value is recommended for use, which is defined as the absorption equivalent thickness (AET). The dependence of AET with depth has been studied for cork from 6-18 MeV by Almond et al. (1967) They define the coefficient of equivalent thickness (CET) and demonstrate the difference between using the AET and CET. It is clear that the reason for the variation of CET with depth and energy is due to the scattering and other physical properties of the electrons, and that some type of modeling of these effects is required to have a general purpose dose calculating system. The current "state-of-the-art" are the pencil-beam algorithms, which can simultaneously consider the effects of range shortening and sidescatter equilibrium.

2. Sidescatter

One of the more neglected but significant processes through which electron beam dosimetry is affected is sidescatter. As electrons pass through a medium, their direction of flight is deflected laterally by multiple Coulomb scattering (MCS) with the nucleus. A monodirectional beam of electrons incident on a thin layer of matter will exit with an angular distribution that is Gaussian with a root-mean-square (RMS) angle given in the Rossi approximation by

$$\theta_{RMS} = \frac{21}{E} \sqrt{\frac{t}{X_o}}, \tag{8}$$

where E is the incident electron energy in MeV, t is the thickness of the layer, and X_o is the radiation length in the material.

As a result of MCS, a significant perturbation of the dose beneath the edge of a lateral discontinuity in tissue can occur. Such areas in the body could be a hard bone, an air cavity, or the irregular surface of the skin such as the nose. To visualize the effect of sidescatter, let us consider the ideal case, as presented by Goitein, (1998) of two thin semi-infinite slabs abutted as shown in Figure A1. At a distance t beneath the slabs the relative planar fluence, which would be approximately proportional to dose, versus position is given by

$$\Phi_p / \Phi_0 = 1 + \tfrac{1}{3} \left[erf\left(\frac{x}{\sqrt{2}\sigma_2} \right) - erf\left(\frac{x}{\sqrt{2}\sigma_1} \right) \right] \tag{9}$$

where σ_1 and σ_2, are the root-mean-square (RMS) spreads of the two materials. Analysis of the curves indicate:

1. The maximum dose perturbation is $\pm$ 50%.
2. For equal ratios (σ_1/σ_2,) the maximum dose perturbation is identical, but its range of influence increases as the sigmas increase.
3. The minimum dose lies under the medium with the greatest sigma, and the maximum dose lies under the medium with the smallest sigma.

In actual cases the dose perturbations are different due to the more complicated nature of the actual situation. Three properties to be considered are: (1) the angular divergence inherent of the initial beam; (2) the presence of additional tissue proximal and distal to the lateral discontinuity; and (3) the irregular nature of the actual discontinuity. The former two effects tend to decrease the magnitude of the dose perturbation as they contribute a constant sigma, which adds RMS to the sigma of the two media, effectively making the ratio of the two sigmas closer to unity. An excellent discussion of this phenomenon is given by Goitein et al. (1978). The influence of irregularly shaped discontinuities is more complicated, and a few select cases have been discussed by Goiten et al.

3. Electron backscatter

Dose at any point in an electron beam is primarily due to electrons traveling with a vector component parallel to the incident beam; however, a small contribution arising from electrons traveling with a vector component antiparallel to the incident beam exists. Such electrons are referred to as backscattered and primarily arise from delta rays undergoing subsequent multiple Coulomb scattering. A quantitative description of this phenomenon is beyond the scope of this paper; however, a discussion of its dosimetric effect is in order.

Early experiments by Almond et al. (1967), measuring the difference between dose in a wax phantom both with wax and with air distal to the chamber located at depth, for 6 MeV electrons showed approximately 10% of the dose is due to backscattered electrons. Similar measurements by Loevinger (1961) showed contributions from 10% to 4% at the depth of maximum dose for initial electron energies from 10 MeV to 40 MeV. Almond et al. (1967) also showed that at most a 2%-3% decrease in dose was observed when the wax distal to the probe was replaced with cork. The smallness of this effect is most likely due to the similar effective atomic numbers of wax and cork and indicates that backscatter from lung is probably not a clinically significant phenomenon. Because air cavities within the body are normally quite small, it should be realized that the 4%-10% dose decreases discussed above are most likely not applicable; in fact, the air cavities within the body probably perturb the dose due to backscatter a clinically insignificant amount, although no data to confirm this statement were found. Therefore, only materials with dissimilar effective atomic numbers such as hard bone, teeth, dental

caps (steel, gold, etc.), and other internal metals are expected to modify significantly the dose near the tissue-high Z material interface.

The effects of backscatter can be summarized as follows:

1. The dose enhancement is maximum at a tissue-high Z interface, and decreases to zero in a nonlinear manner (approximately exponentially) at a depth several millimeters proximal to the interface (Gagnon and Cundiff, 1980). A detailed parameterization of electron backscatter versus depth proximal to a tissue-lead interface has been made by Lambert and Klevenhagen (1982). This distance from the interfaces ranges from 1.3 cm to 2.0 cm for electrons with an average energy from 7 MeV to 12 MeV for Lipowitz alloy (Z_{eff}=75) and from 1.0 cm to 2.0 cm for the same electron energies in titanium (Z=22).

2. The measure of dose enhancement is the electron backscatter factor (EBF), which is the ratio of the dose at the interface to that which would result if the high-Z material were replaced by tissue. This factor is found to decrease with increasing energy and to be relatively independent of the electron energy distribution, depending only on the average energy, $\overline{E}_z$. For lead, Klevenhagen et al. 1982) have shown

$$EBF = 1 + 0.735\exp(-0.052\,\overline{E}_z), \qquad (10)$$

where $\overline{E}_z = \overline{E}_o$ (1-z/R_p), $\overline{E}_o$ is the incident kinetic energy, z is the depth, and R_p is the practical range.

3. The electron backscatter factor is found to increase with increasing atomic number (z), and Klevenhagen et al. (1982) have shown their data to be fit by the expression.

$$EBF = A - B\exp(-kZ), \qquad (11)$$

where (A, B, k) are energy dependent and equal (1.95, 1.03, 0.0145), (1.98, 1.03, 0.0072), and (2.0, 1.02, 0.0039) at 4.6 MeV, 9.1 MeV, and 19.2 MeV, respectively.

4. The electron backscatter factor also depends on the scatter thickness. Approximately 99% of full backscatter is achieved by 0.7 gm/cm^2 of pressed wood (Loevinger et al., 1961). A more precise measurement in lead has been made by Klevenhagen et al. (1982) showing the scatter thickness to achieve 99% of full backscatter to be energy dependent and given by

$$t(gm/cm^2) = 0.16\,\overline{E}_z(MeV). \qquad (12)$$

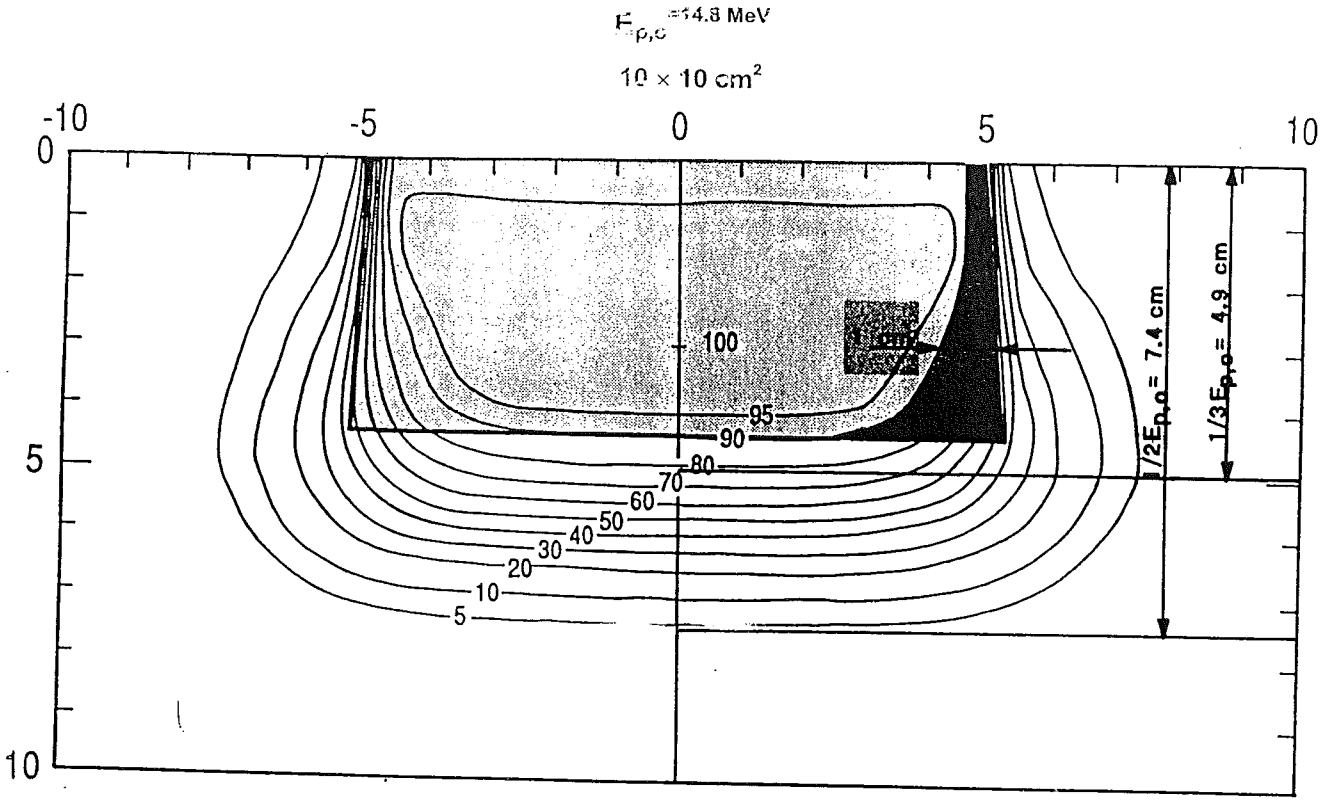

Figure 1. Electron dose distribution in water resulting from a 15-MeV electron beam of normal incidence.

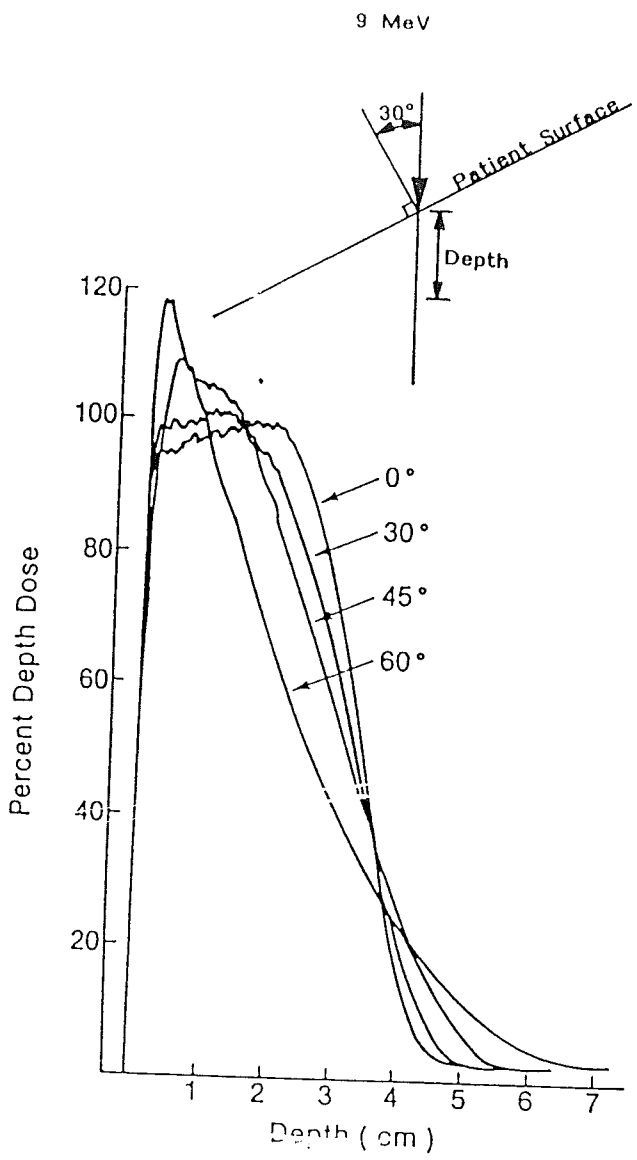

Figure 2. Comparison of central-axis depth dose for a 9-MeV beam incident at various angles (0°-6°) from normal isodose (from Ekstrand and Dixon, 1982).

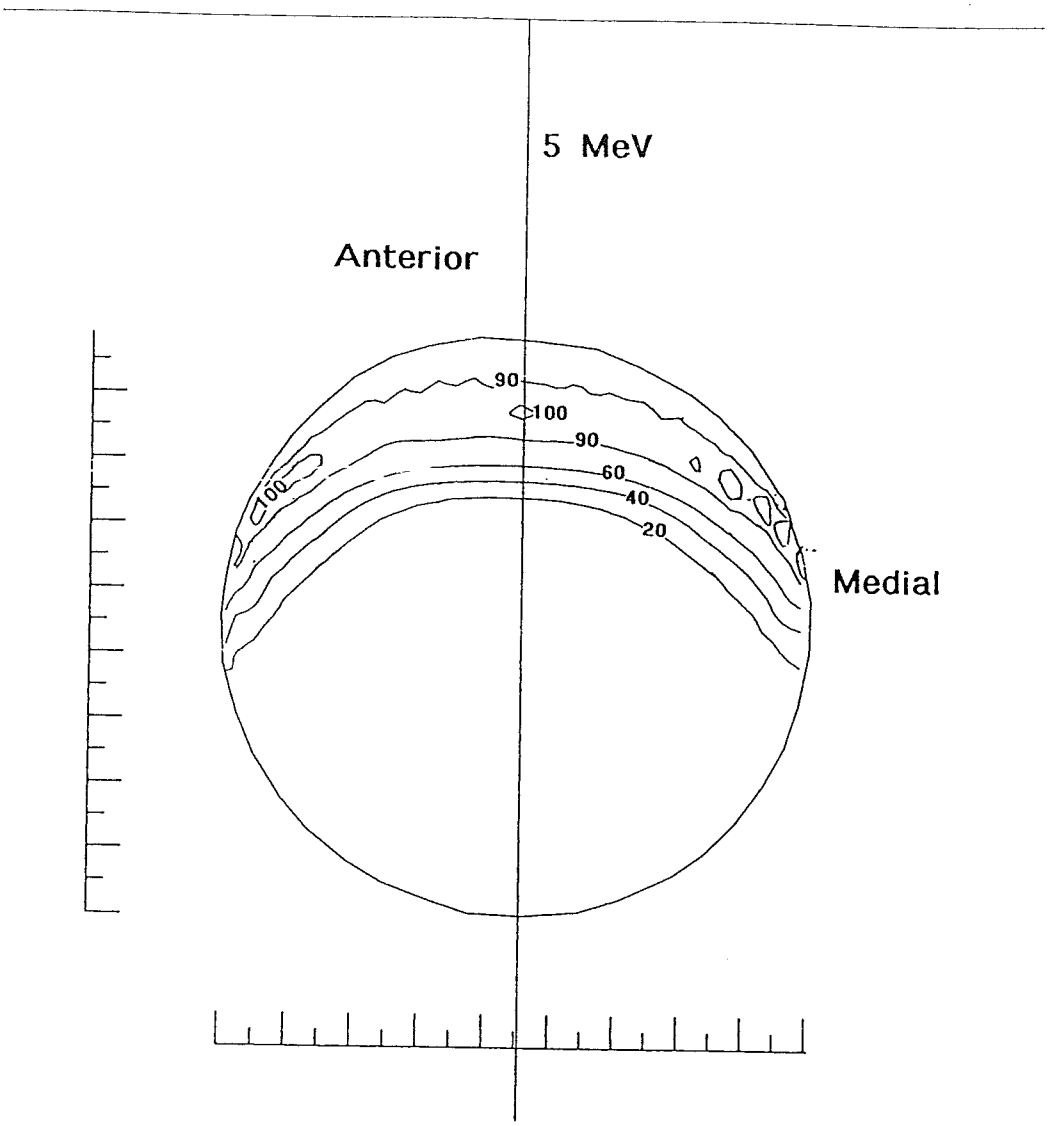

Figure 3. Pencil-beam calculated dose distribution resulting from a broad 5-MeV electron beam irradiating a 9-cm diameter cylinder simulating a patient's calf.

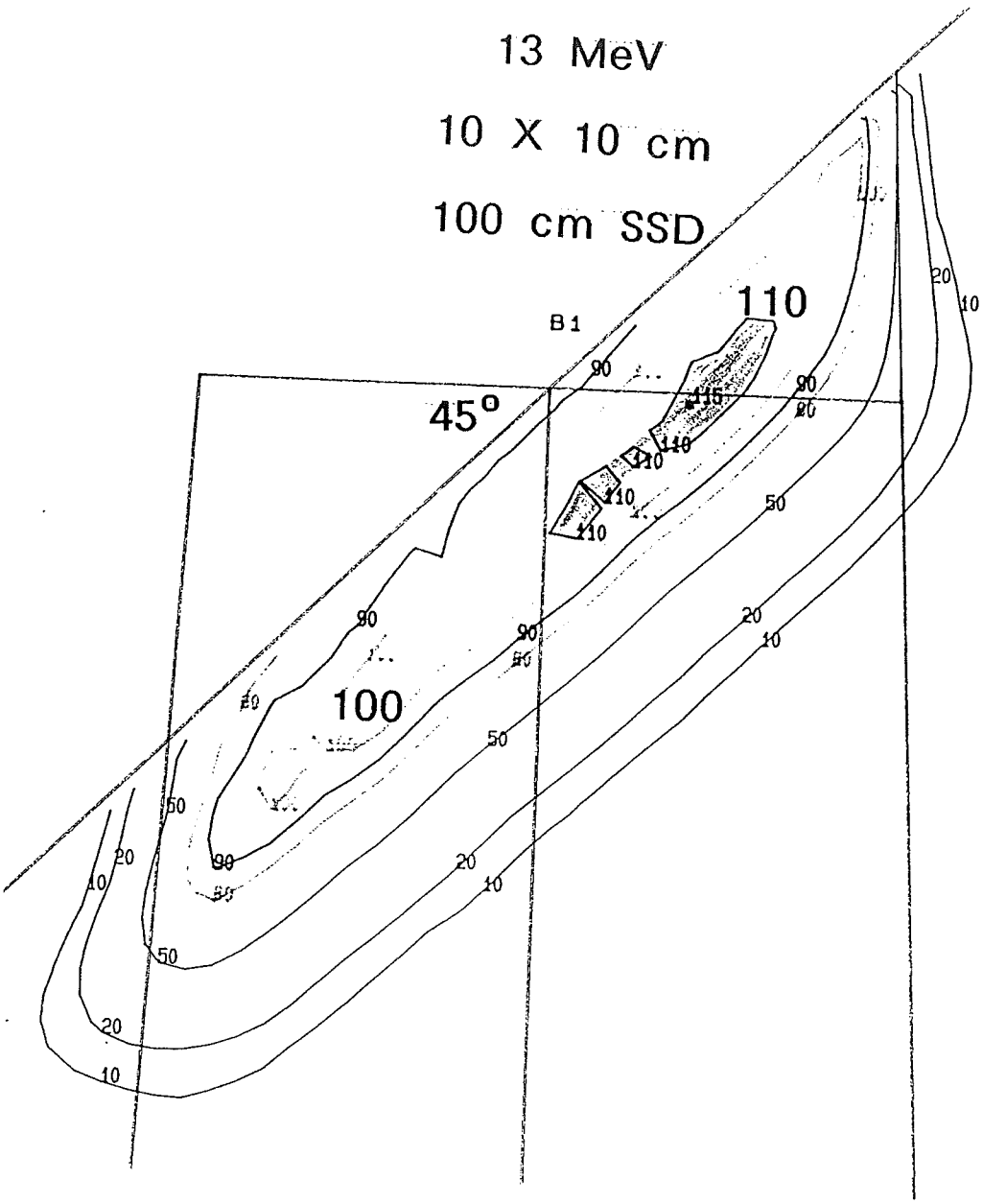

Figure 4. Pencil-beam calculated dose distribution in water resulting from a 13-MeV electron beam incident at 45° from the normal.

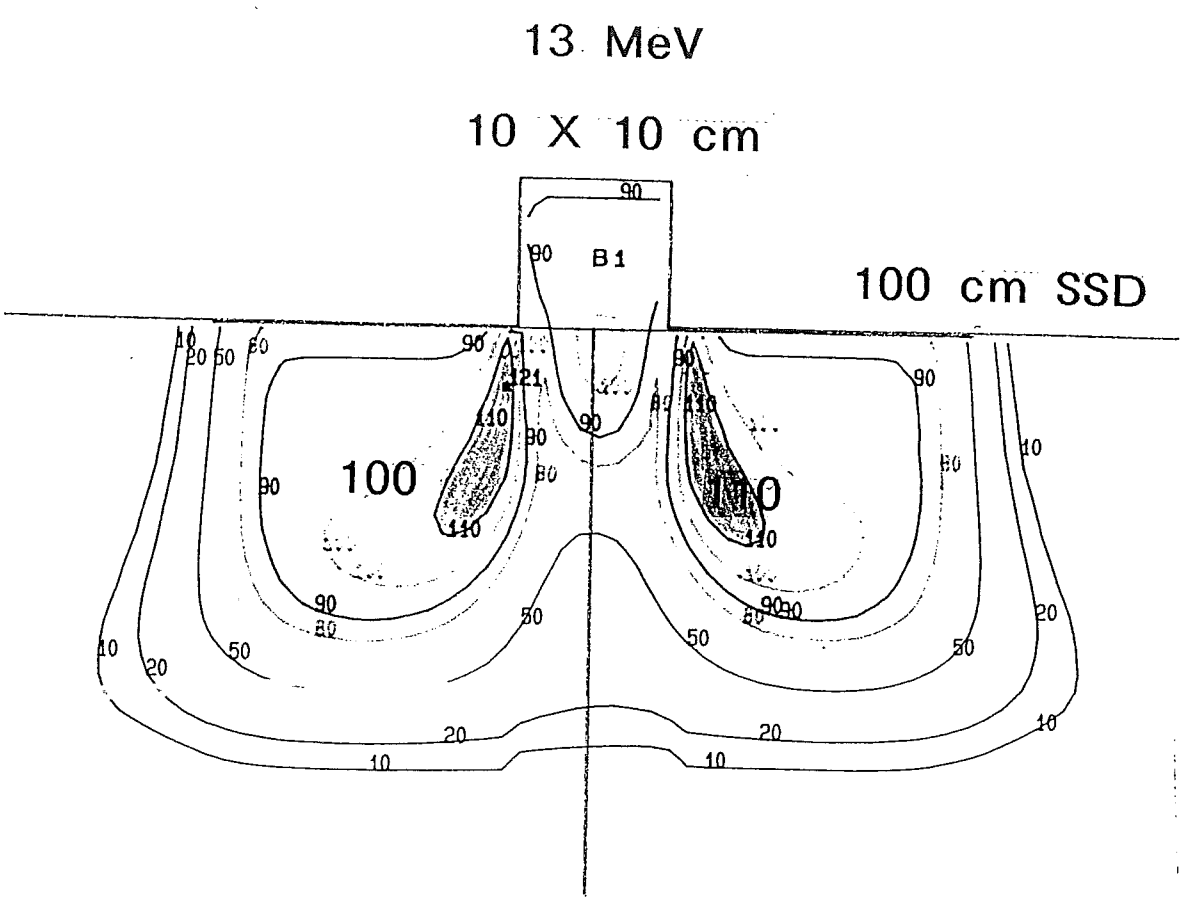

Figure 5. Pencil-beam calculated dose distribution resulting from a 13-MeV electron beam incident on a water phantom having a long protrusion with a 2×2 cm^2 cross section.

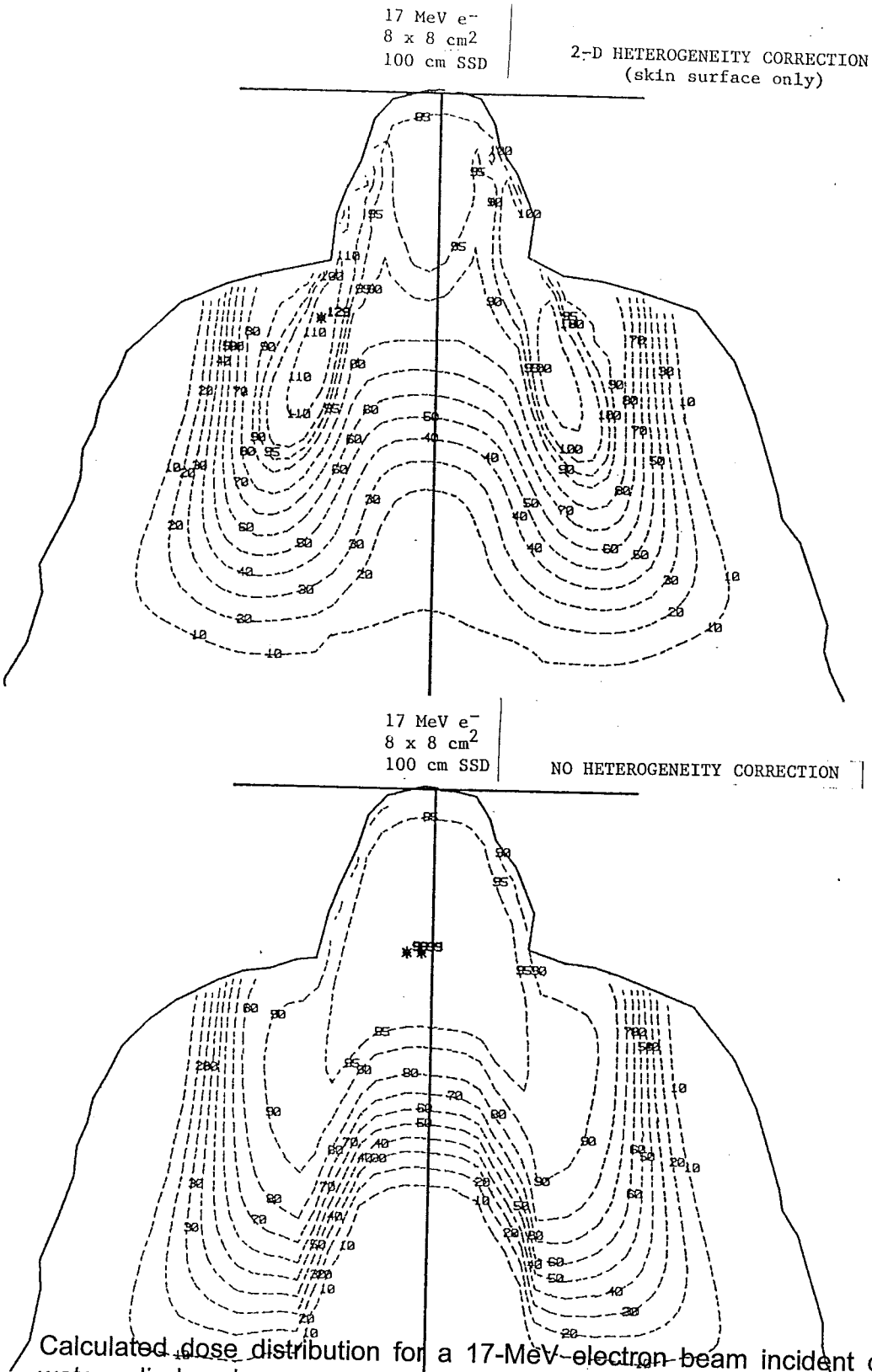

Figure 6. Calculated dose distribution for a 17-MeV electron beam incident on a water cylinder whose cross-section is taken from a patient's transverse CT scan. (A) the 2D pencil-beam algorithm shows the effect of scatter in creating hot/cold spots in the dose distributions. (B) the 1D pencil-beam ignores lateral scatter producing a dose distribution void of actual hot/cold spots.

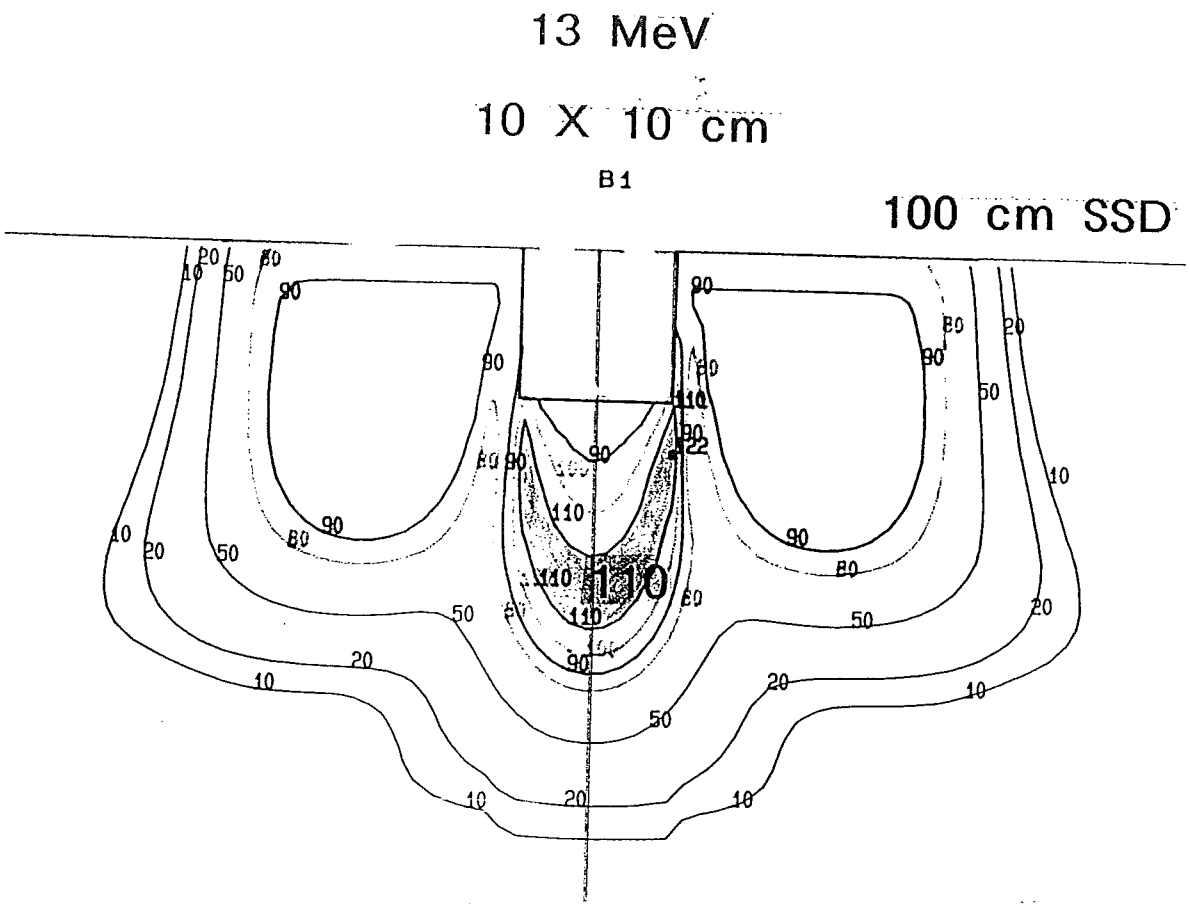

Figure 7. Pencil-beam calculated dose distribution resulting from a 13-MeV electron beam incident on a water phantom having a long depression with a 2×2 cm^2 cross section.

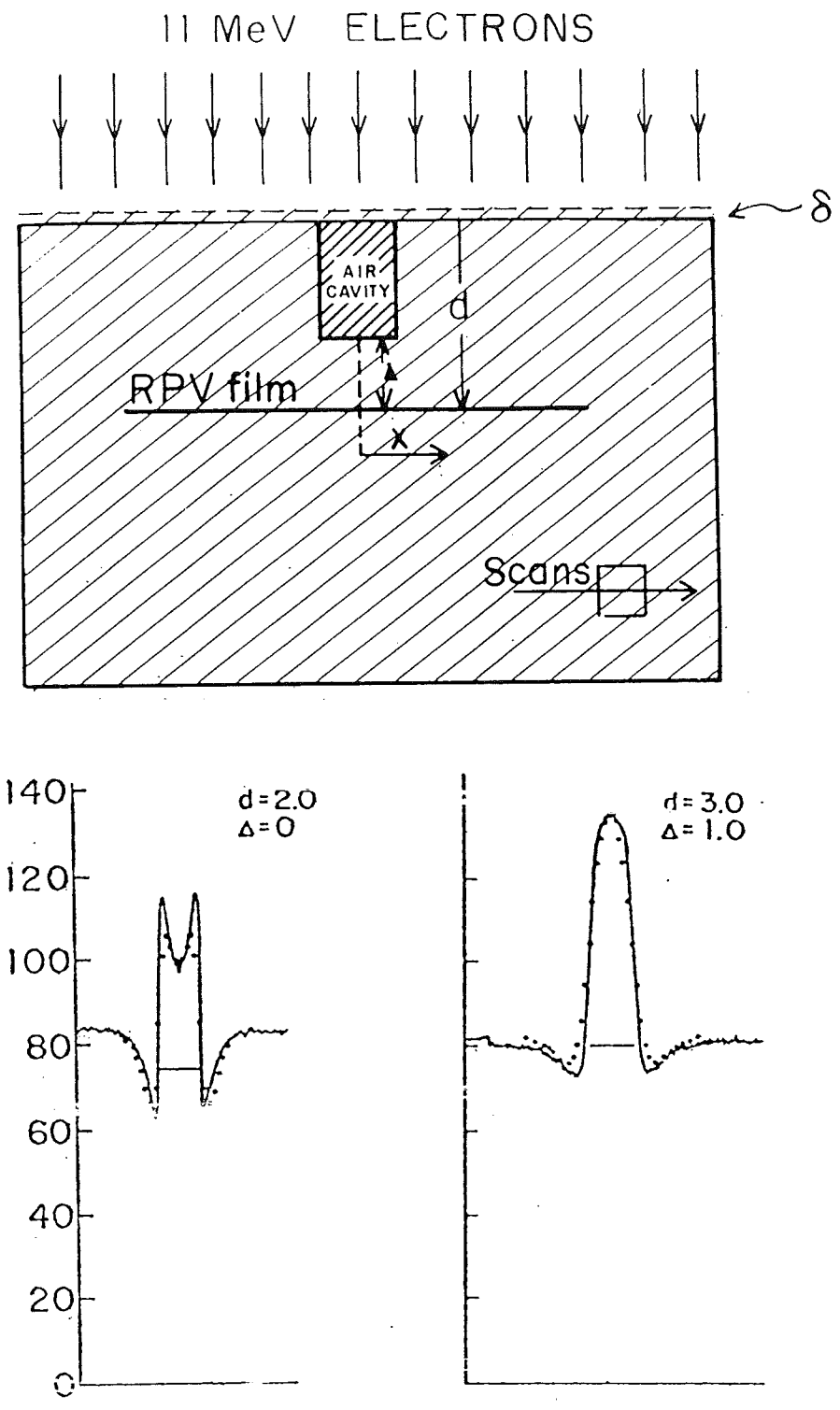

Figure 8. (A) Geometry for a 11-MeV electron beam irradiating a $1\times1\times2$ cm^2 air cavity. (B) Dose profiles at a distance 0 and 1.0 cm below the cavity.

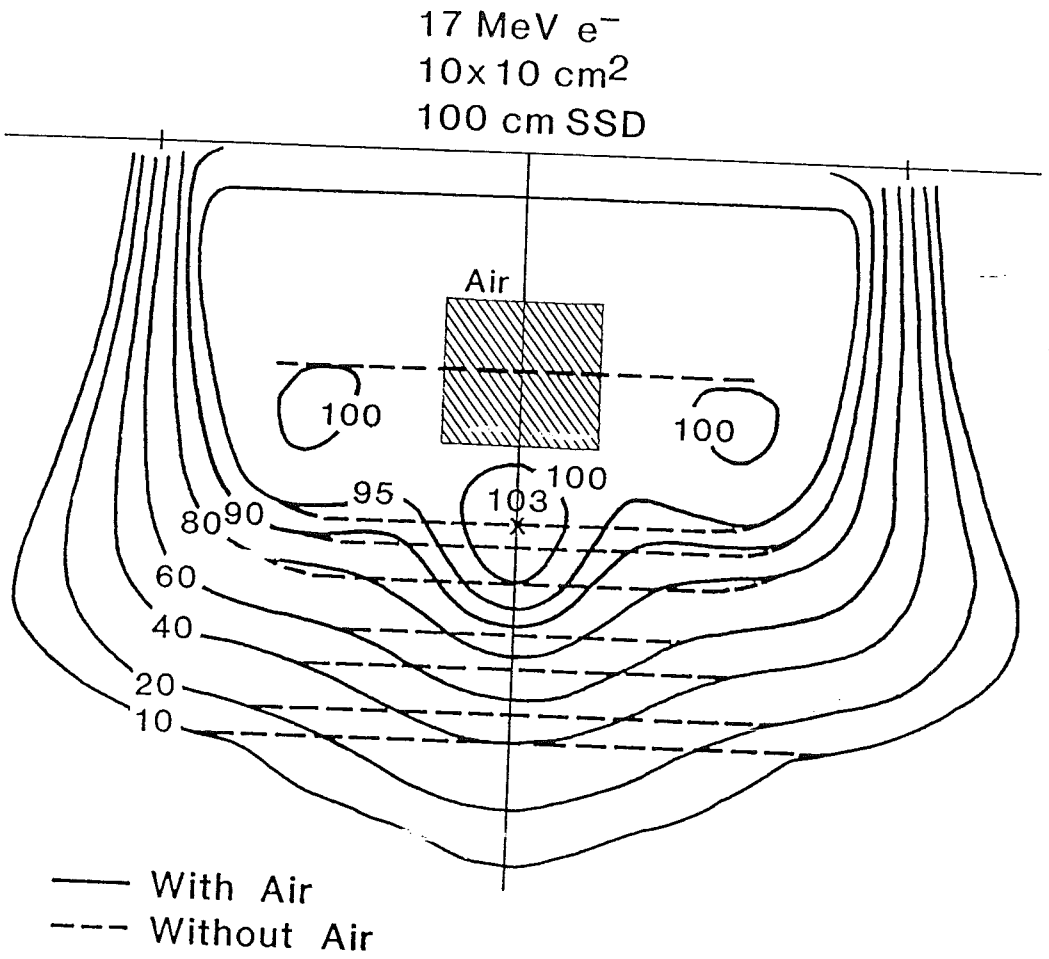

Figure 9. Comparison of pencil-beam calculated dose distributions in a semi-infinite water slab with that of a semi-infinite water slab containing a long air cavity with a 2 × 2 cm^2 cross-section located 2 cm below the surface.

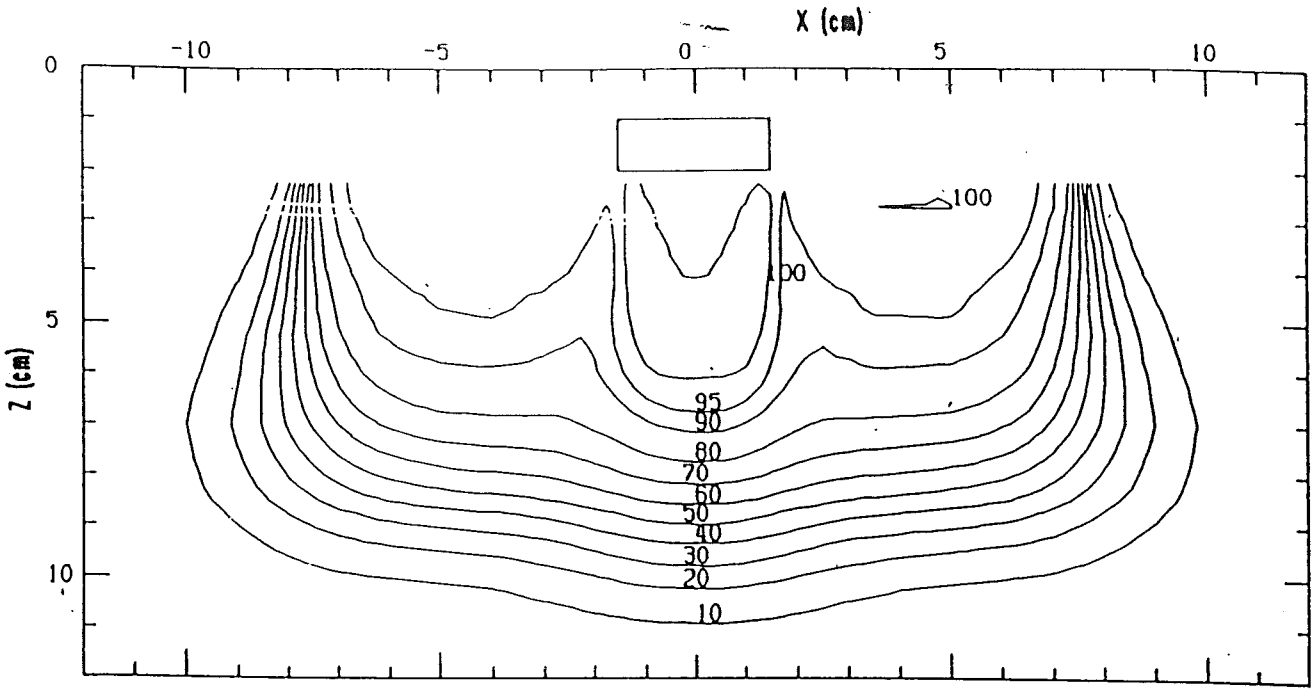

Figure 10. Measured dose distribution for a 20-MeV electron beam incident on a water phantom containing an air cylinder with a 1×2 cm^2 cross section, 1 cm below the surface (Shiu et al., 1992).

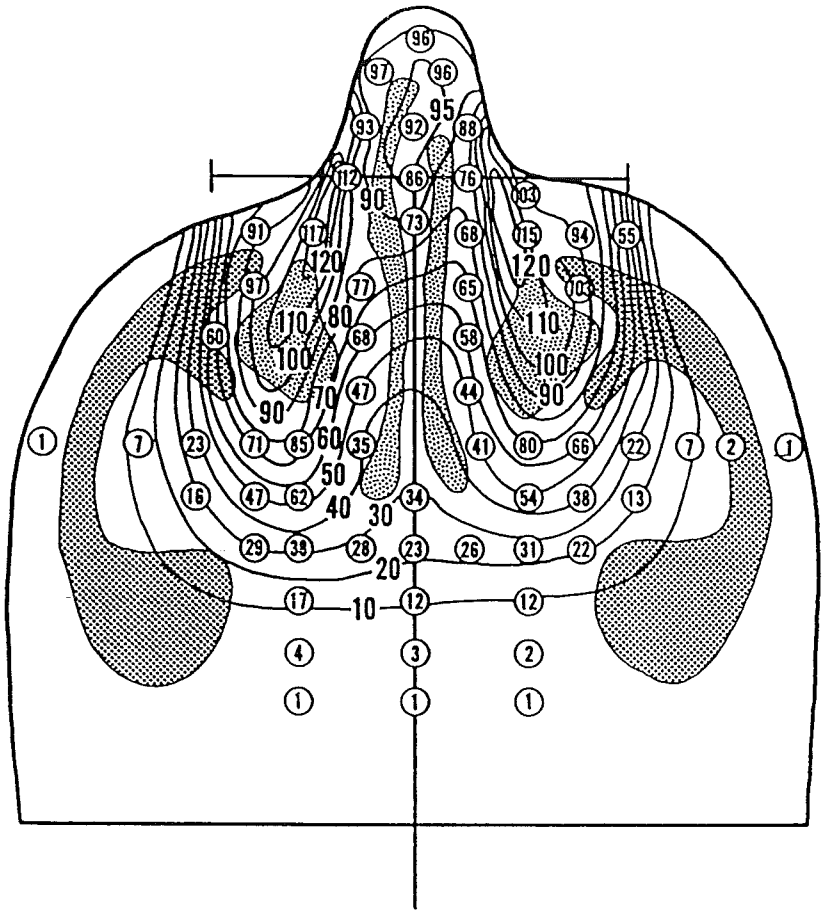

Figure 11. Comparison of pencil-beam calculated dose distribution (solid curves) with measured dose points for a 13 MeV electron beam incident on a right cylindrical phantom containing bone and air with a cross-section modeled after a patient's transverse CT scan (from Hogstrom et al., 1983).

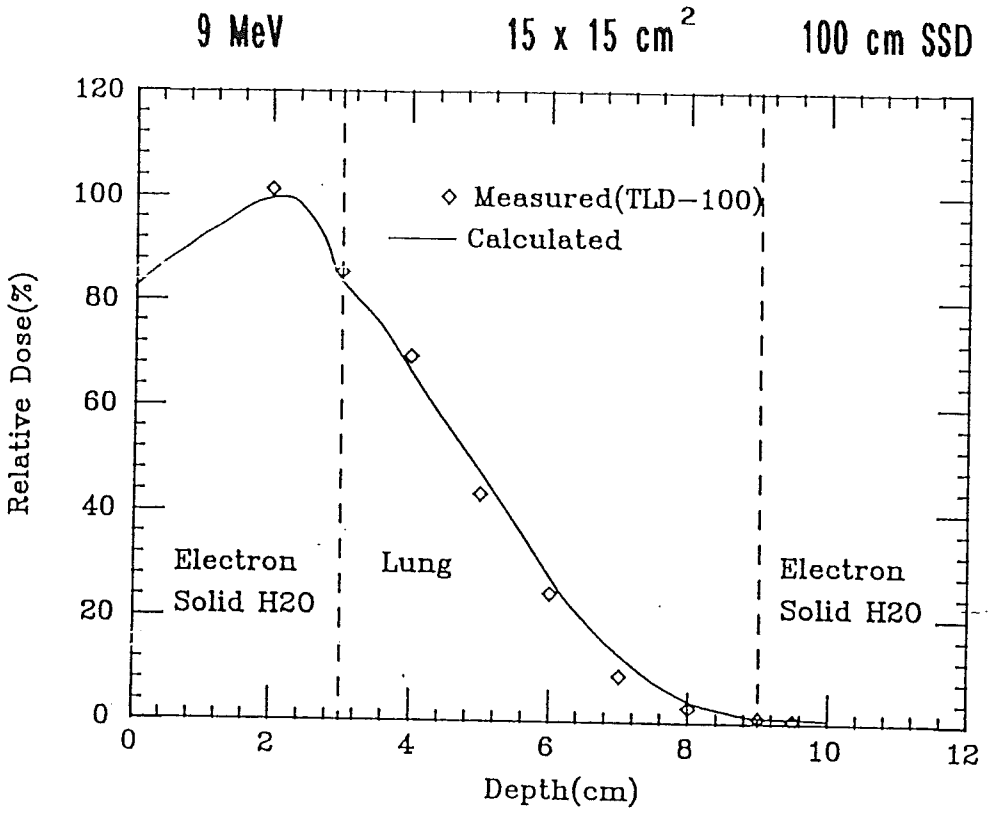

Figure 12. Central-axis depth dose measured with TLD in a 1D phantom containing electron solid water and lung substitute (from Shiu et al., 1992). The solid curve represents the depth dose calculated using a pencil-beam algorithm.

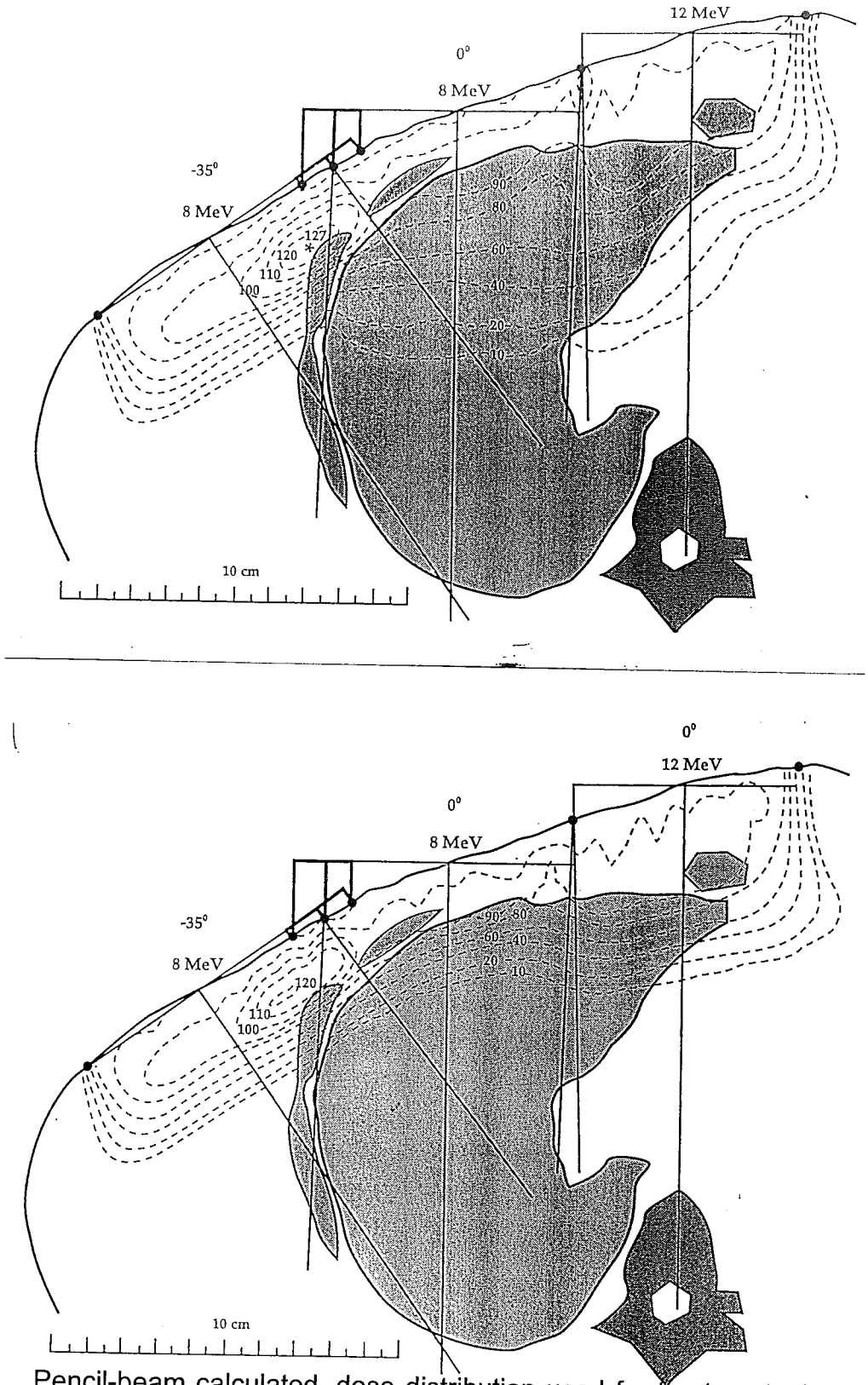

Figure 13. Pencil-beam calculated, dose distribution used for treatment of the chest wall. The IMC field uses a 12-MeV electron beam and the chest wall fields use an 8-MeV electron beam. The boundary between the chest wall fields is feathered ± 1 cm. (A) Dose calculated on a pixel by pixel basis accounting for patient heterogeneity. (B) Dose calculated assuming patient anatomy is water.

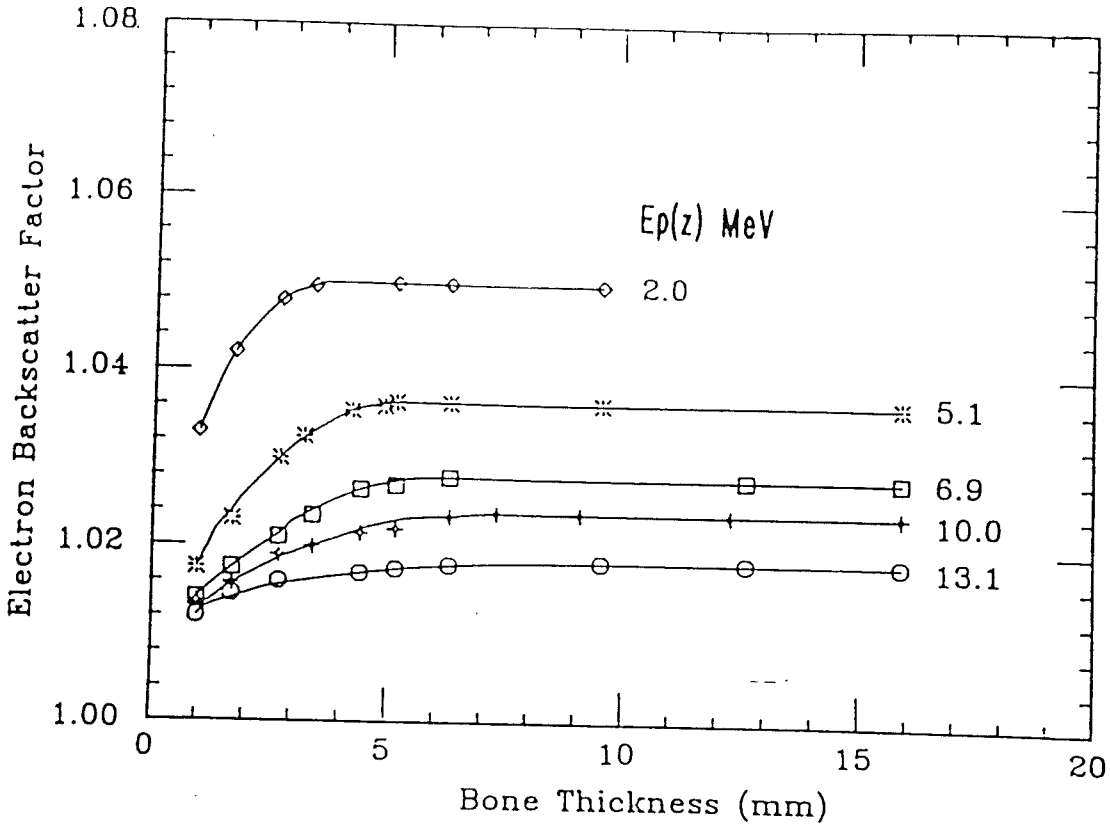

Figure 14. Electron backscatter factor versus bone thickness for electrons with a most probable energy ranging from 2.0 to 13.1 MeV (from Shiu and Hogstrom, 1992).

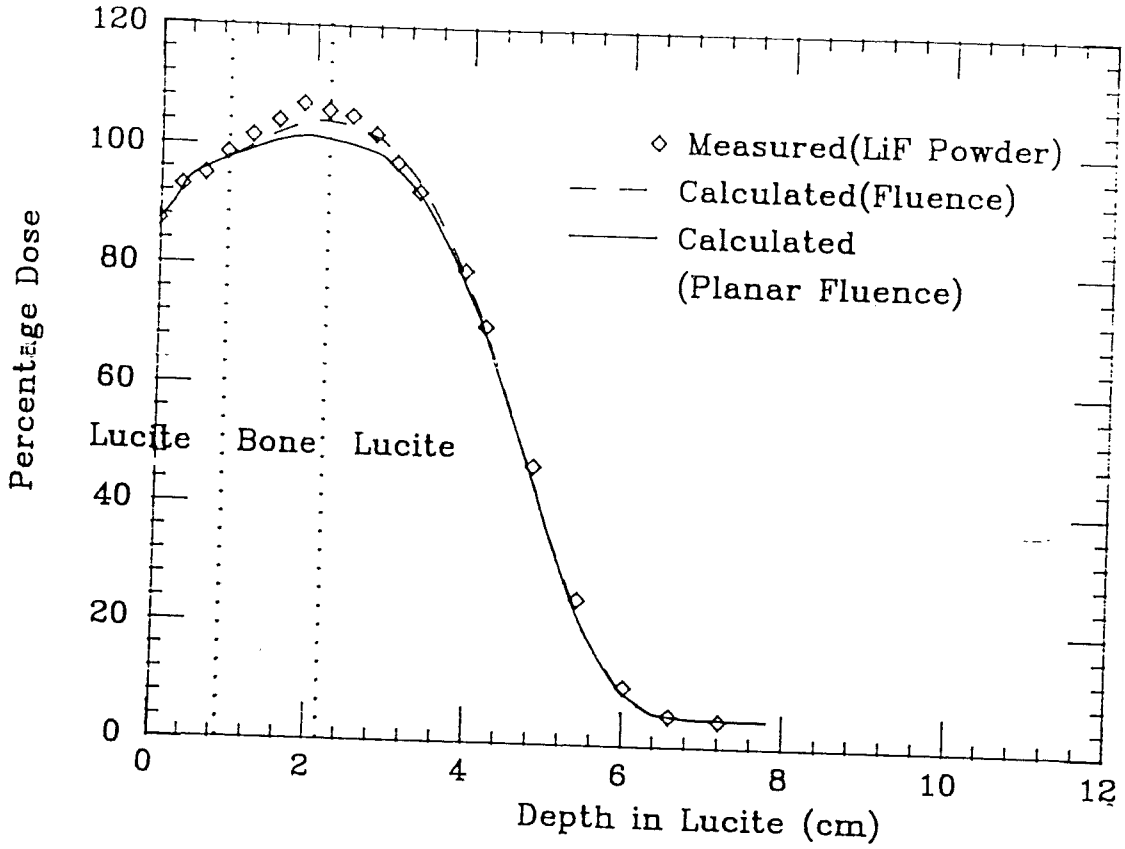

Figure 15. Measured depth dose resulting from a 15-MeV electron beam incident on a PMMA-Bone-PMMA phantom, in which the 1.3-cm thick bone is 0.9 cm below the surface (from Shiu and Hogstrom, 1991).

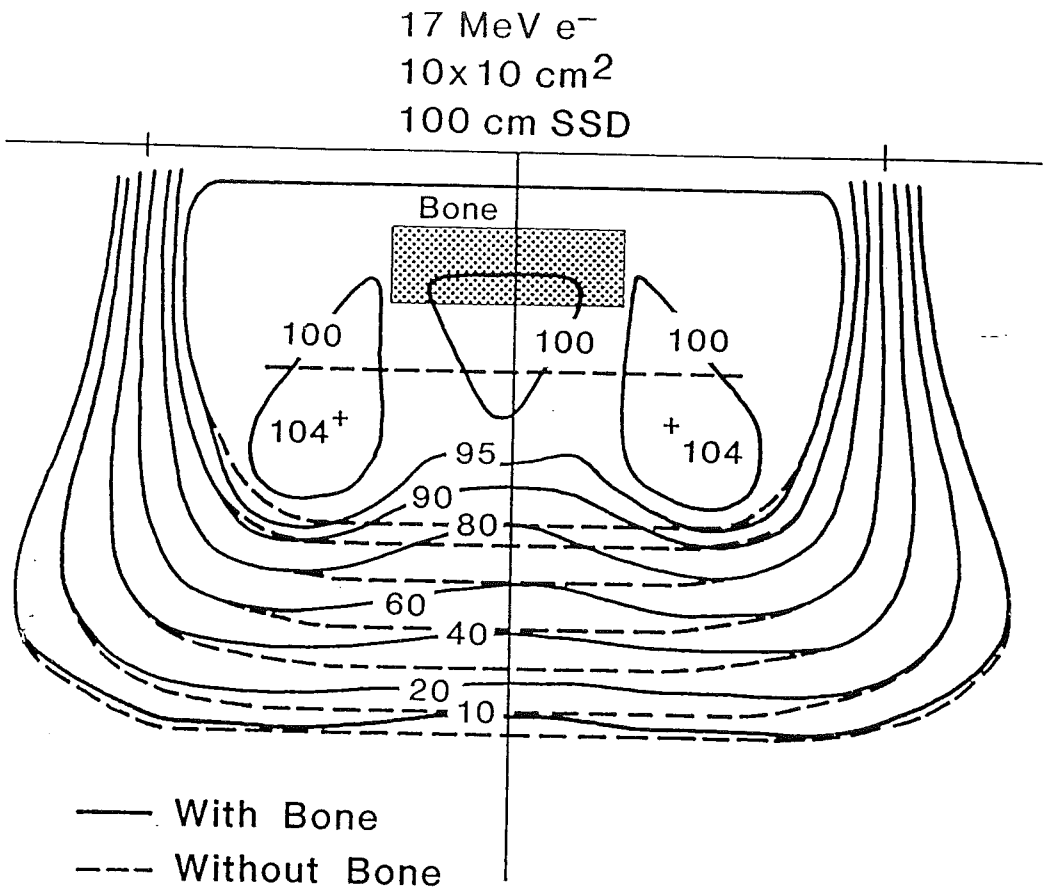

Figure 16. Comparison of pencil-beam calculated dose distributions in a semi-infinite water slab with that of a semi-infinite water slab containing a bone cylinder with a 1 × 3 cm^2 cross-section located 1 cm below the surface.

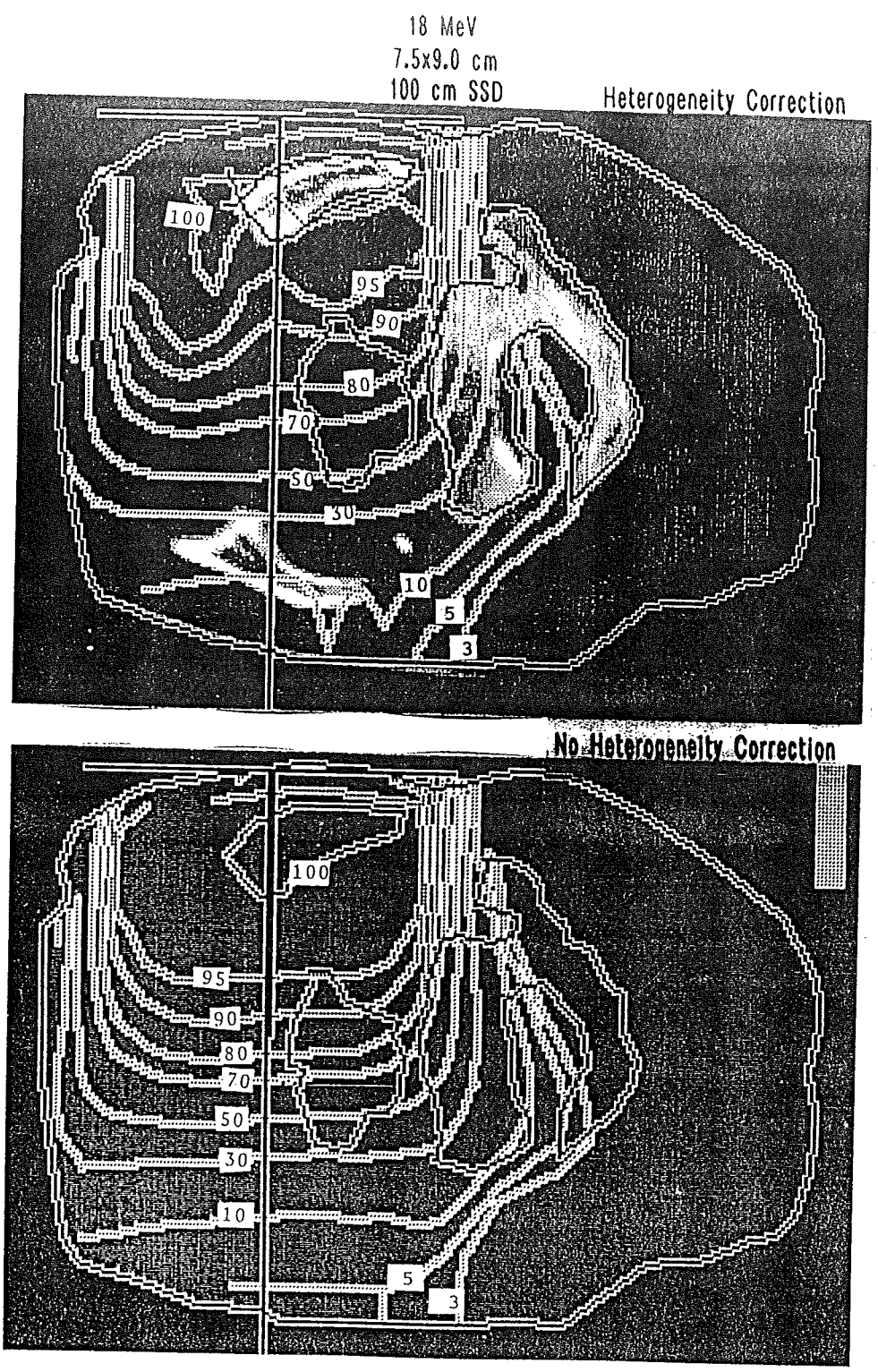

Figure 17. Comparison of 2D pencil-beam calculated dose distributions for a transverse patient plane. An 18-MeV electron beam used to treat carcinoma of the buccal mucosa and retromolar trigone. (A) Pixel by pixel correction made for patient anatomy. (B) Patient is assumed to be water, i.e., tissue heterogeneity ignored.

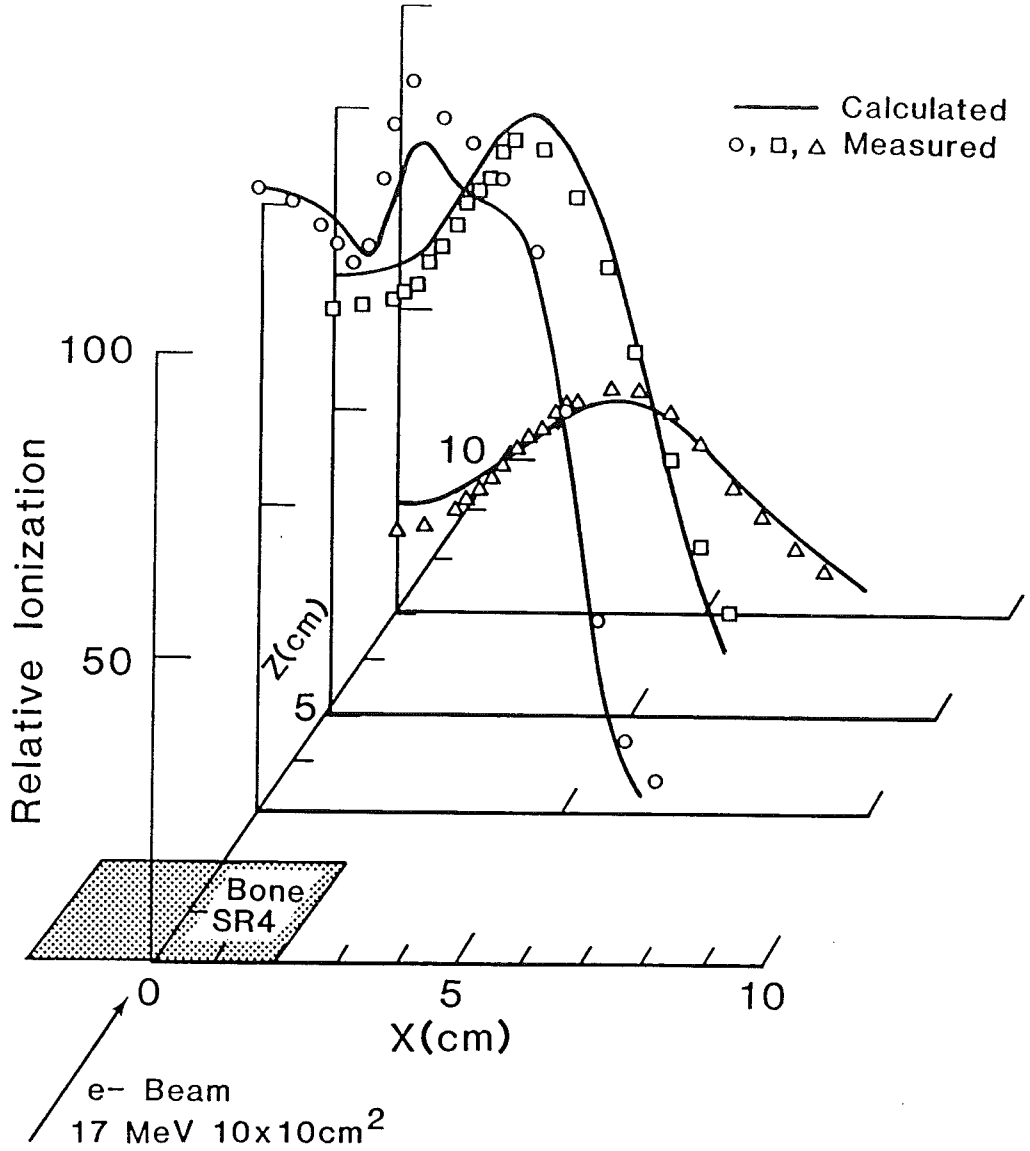

Figure 18. Off-axis dose plate for a 17-MeV electron beam 1-, 3-, and 5-cm behind a 2-cm thick SR4 bone. The bone cross-section is 2×4 cm^2. The symbols are measured data; the solid lines are calculated using the pencil-beam dose algorithm (from Hogstrom et al., 1981).

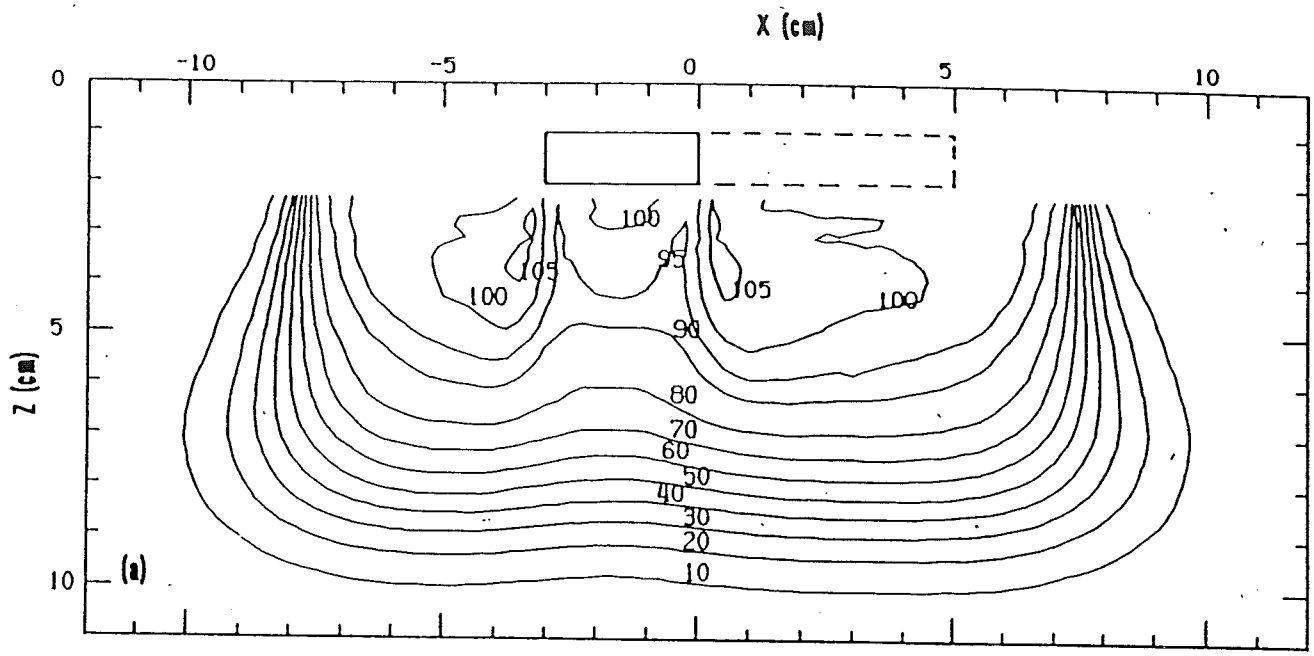

Figure 19. Measured dose distribution for a 20-MeV electron beam incident on a water phantom containing an L-shaped bone (1×2 cm^2 cross section) 1 cm below the surface, which simulates the mandible (from Shiu et al., 1992).

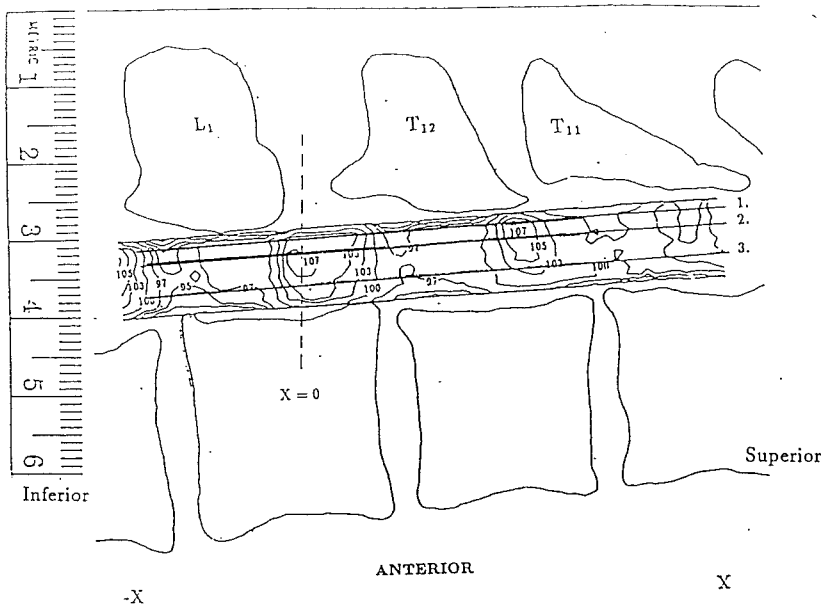

1. Average Depth = 3.0 cm
2. Average Depth = 3.2 cm
3. Average Depth = 3.6 cm

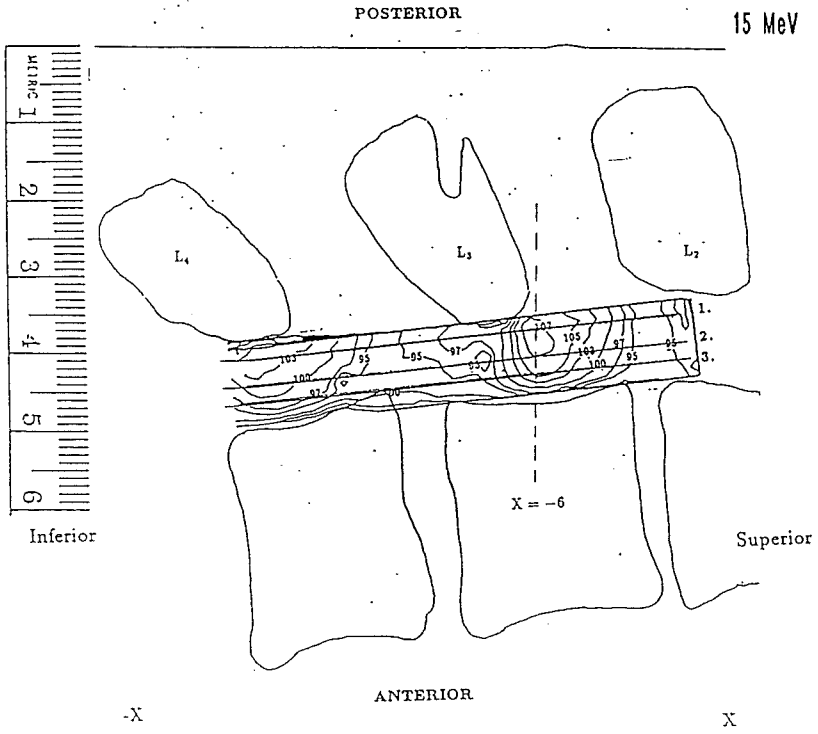

1. Average Depth = 3.8 cm
2. Average Depth = 4.2 cm
3. Average Depth = 4.4 cm

Figure 20 Measured dose distribution in mid-sagittal plane of spinal cord for 15 MeV electron beam used to irradiate a muscle equivalent phantom in which a rehydrated spinal column was embedded. Dose distribution is shown (A) from T11-L1 and (B) from L2-L4 (from Dominiak, 1991).

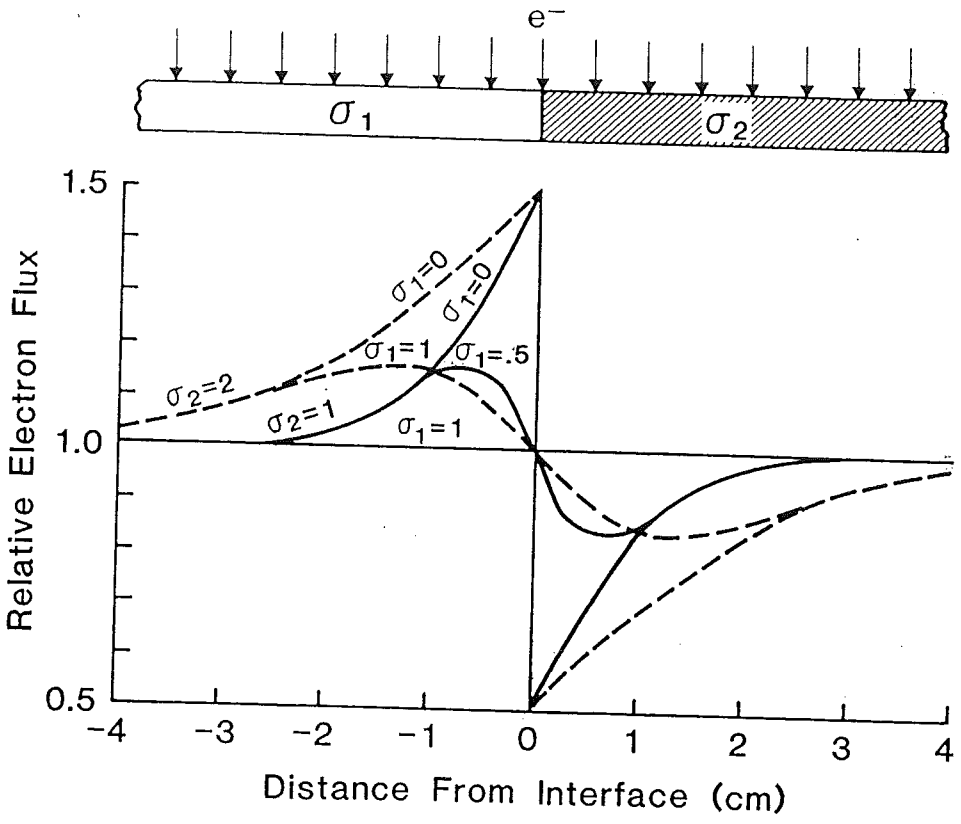

Figure A-1. Plot of electron planar fluence beneath the interface of two semi-infinite slabs with differing linac angular scattering powers illustrates the hot/cold spots that results from loss of side scatter equilibrium. σ_i is the RMS value of the scattering distribution from the ith slab at the plane of measurement. This is the basis for hot/cold spots in patients that are generated by lateral discontinuities in the anatomy.

REFERENCES

Almond P.R. High-energy electron dose perturbations in regions of tissue heterogeneity. II. Physical models of tissue heterogeneities. Radiology, 88:1146-1153, 1967.

Dominiak G.S. Dose in spinal cord following electron irradiation (M.S. thesis). The University of Texas Health Science Center at Houston, Graduate School of Biomedical Sciences, 1991.

Ekstrand K.E. and Dixon R.L. The problem of obliquely incident beams in electron-beam treatment planning. Medical Physics, 9:276-278, 1982.

Fields R.S. and Hogstrom K.R. Optimization of electron-photon mixed beam planning. In: Proceedings of Eighth International Conference on the Use of Computers in Radiation Therapy, pp. 248-254, Silver Spring; IEEE Computer Society Press, 1984.

Gagnon W.F. and Cundiff J.H. Dose enhancement from backscattered radiation at tissue-metal interfaces irradiated with high energy electrons. Br J Radiol, 53:466-470, 1980.

Goitein M., Chen G.T., Ting, J.Y., Schneider R.J., and Sisterson J.M. Measurements and calculations of the influence of thin inhomogeneities on charge particle beams. Medical Physics 5:265-273, 1978.

Hogstrom K.R. Dosimetry of electron heterogeneities. In: A. Wright and A. Boyer (eds.), Medical Physics Monograph No. 9: Advances in Radiation Therapy Treatment Planning, pp. 223-243, New York; American Institute of Physics, 1983.

Hogstrom K.R. Treatment planning in electron-beam therapy. In: J.M. Vaeth and J.L. Meyer (eds.), Frontiers in Radiation Therapy Oncology: The Role of High Energy Electrons in the Treatment of Cancer, pp. 30-52, Farmington, CT; S. Karger Publisher, Inc., 1991.

Hogstrom K.R. Clinical electron beam dosimetry: basic dosimetry data. In: J. Purdy (ed.), Advances in Radiation Oncology Physics - 1990 Proceedings of the Summer School of the AAPM, pp. 390-429, New York; American Institute of Physics, 1991.

Hogstrom K.R. and Steadham R.S. Electron beam dose computation. In: J. Palta and T. R. Mackie (ed.), Teletherapy: Present and Future - 1996 Proceedings of the Summer School of the AAPM, pp. 137-174, Vancouver: Advanced Medical Publishing, 1996.

Hogstrom K.R., Mills M.D., and Almond P.R. Electron beam dose calculations. Physics in Medicine and Biology, 26:445-459, 1981.

Hogstrom K.R., Mills M.D., Meyer J.A., Palta J.R., Mellenberg D.E., Meoz R.T., and Fields R.S. Dosimetric evaluation of a pencil-beam algorithm for electrons employing a two-dimensional heterogeneity correction. International Journal of Radiation Oncology Biology Physics, 10:561-569, 1983.

ICRU Report 35. Radiation Dosimetry: Electron Beams with Energies Between 1 and 50 MeV. Bethesda: International Commission on Radiation Units and Measurements, 1984.

Johns H.E. and Cunningham J.B. The Physics of Radiology. 4th ed. Springfield, IL: Charles C. Thomas, 1983.

Kirsner S.M., Hogstrom K.R., Kurup R.G., and Moyers M.F. Dosimetric evaluation in heterogeneous tissue of anterior electron beam irradiation for treating retinoblastoma. Medical Physics, 14(5):772-779, 1987.

Klevenhagen S.C., Lambert G.D., and Arbabi A. Backscattering in electron beam therapy for energies between 3 and 35 MeV. Phys Med Biol, 27:363-373, 1982.

Lambert G.D. and Klevenhagen S.C. Penetration of backscattered electrons in polystyrene for energies between 1 and 25 MeV. Phys Med Biol, 27:721-725, 1982.

Laughlin J.S., Lundy A., Phillips R., Chu F., and Sattar A. Electron-beam treatment planning in inhomogeneous tissue. Radiology, 85:524-531, 1965.

Loevinger R., Karzmark C.J., and Weissbluth M. Radiation therapy with high-energy electrons. Radiology, 77:906-926, 1961.

Maor M.H., Fields R.S., Hogstrom K.R., and Van Eys J. Improving the therapeutic ratio of craniospinal irradiation in medulloblastoma. International Journal of Radiation Oncology Biology Physics, 11:687-707, 1985.

McKenzie A.L. Air-gap correction in electron treatment planning. Phys Med Biol, 24:628-635, 1979.

Morrison W.H., Wong P.F., Starkschall G., Garden A.S., Childress C, and Hogstrom, K.R. Water bolus for electron irradiation of the ear canal. International Journal of Radiation Oncology Biology Physics, 33(2):479-483, 1995.

Perry D.J. and Holt J.G. A model for calculating the effects of small inhomogeneities on electron beam dose distributions. Medical Physics, 7:207-215, 1980.

Prasad S.C., Ames T.E., Howard T.B., Bassano D.A., Chung C.T., King G.A., and Sagerman R.H. Dose enhancement in bone in electron beam therapy. Radiology, 151:513-516, 1984.

Pohlit W. Calculated and measured dose distributions in inhomogeneous materials and in patients. Ann N Y Acad Sci, 161:189-197, 1969.

Shiu A.S. and Hogstrom K.R. Dose in bone and tissue near bone-tissue interface from electron beam. International Journal of Radiation Oncology Biology Physics, 21:695-702, 1991.

Shiu A.S., Tung S., Hogstrom K.R., Wong J.W., Gerber R.L., Harms W.B., Purdy J.A., Ten Haken R.K., McShan D.L., and Fraass, B.A. Verification data for electron beam dose algorithms. Medical Physics, 19:623-636, 1992.

Tapley N.duV. Clinical Applications of the Electron Beam. New York: John Wiley & Sons, 1976.

Wooden K.K., Hogstrom K.R., Blum P., Gastorf R.J., and Cox J.D. Whole-limb irradiation of the lower calf using a six-field electron technique. Medical Dosimetry, 21:211-218, 1996.